4 Results

4.1 Tensile Data

Tensile tests were performed in an Instron tensile test machine in air at 316°C and a strain rate of $\approx 4 \times 10^{-4}$ s^{-1} in accordance with ASTM Specifications E8 and E21. The cross–head movement and digitized load were recorded as a function of time. The strain was calculated based on the cross–head deflection.

4.1.1 Alloy 600 from CRDM Nozzle #3 and Alloy 182 from the Nozzle #11 J–Groove Weld

The engineering stress vs. strain curves for Alloy 600 from the Davis–Besse CRDM Nozzle #3 are shown in Fig. 34, and those for Alloy 182 from Nozzle #11 J–groove weld are shown in Fig. 35. The values of yield and ultimate stresses, elongation, and reduction in area are given in Table 8. The stress vs. strain curves for the three Alloy 600 specimens from the nozzle show excellent agreement (Fig. 34). The results for the Alloy 182 specimens from the J–groove weld show some differences, which are caused either by flaws in the material or the entire gauge length not consisting of the weld metal alone in the specimen.

Table 8. Tensile test results at 316°C for Alloys 600 and 182 removed from the Davis-Besse CRDM nozzle and J–groove weld.

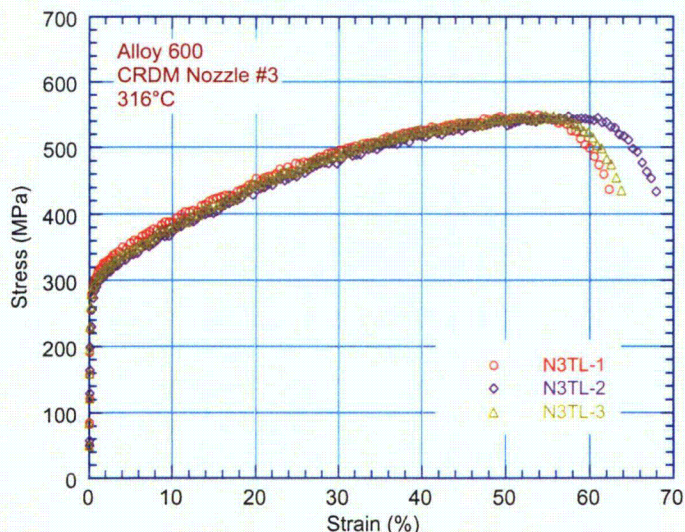| Specimen ID (Alloy Type)	0.2% Yield Stress (MPa)	Ultimate Stress (MPa)	Elongation (%)	Reduction in Area (%)
N3TL-1 (A 600)	290	549	62.3	51.8
N3TL-2 (A 600)	250	548	67.9	54.1
N3TL-3 (A 600)	283	549	63.8	54.0
J11TC-1 (A 182)	390	580	24.6	38.4
J11TC-2 (A 182)	420	587	24.6	58.2
J11TL-2 (A 182) sub–size	346	555	47.8	47.3
J11TL-3 (A 182) sub–size	356	532	36.6	38.0
J11TL-4 (A 182) sub–size	350	420	11.8	14.1

Figure 34.
Engineering stress vs. strain curve at 316°C for Alloy 600 from Davis-Besse CRDM Nozzle #3 in the "L" orientation.
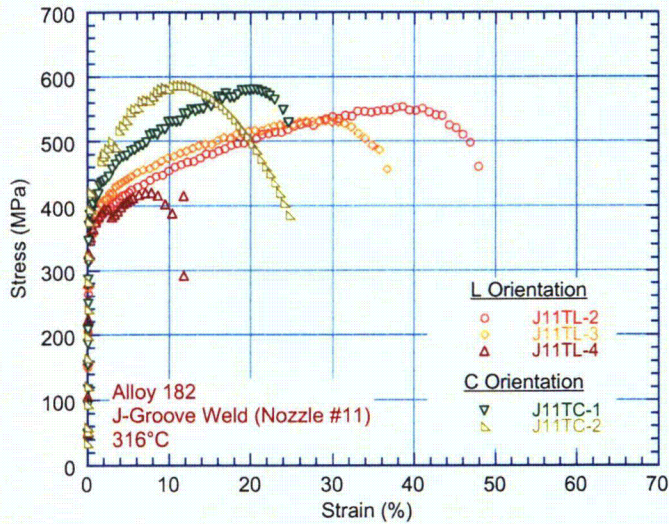
33

Figure 35.
Engineering stress vs. strain curves at 316°C for Alloy 182 from the Davis-Besse CRDM Nozzle #11 J–groove weld in "L" and "C" orientations.

The stress vs. strain curves for two Alloy 182 specimens in the L orientation are comparable (J11TL-2 and -3), but the third specimen (J11TL-4) showed poor ductility because of a large flaw (Fig. 36 a). The stress vs. strain curves for Alloy 182 specimens in the C orientation are significantly different from those in the L orientation. The gauge section near the specimen shoulder of C-orientation specimens contained a small region of the reactor vessel head material. In both C-orientation specimens, fracture occurred in this region; e.g., half of the fracture surface is low–alloy steel in J11TC-1 (Fig. 36b) and all of the fracture surface in J11TC-2 (Fig. 36c). In Specimen J11TC–1, because the soft and hard regions appear to be parallel and approximately of similar areas on the cross section, its stress–vs.–strain curve should be representative of the tensile behavior of the J–groove Alloy 182 in the C orientation. The total elongation for Specimen J11TC–2 can probably not be considered representative.

The tensile strength of the Alloy 182 J–groove weld is higher and the ductility is lower than the corresponding properties for the Alloy 600 nozzle material. For the Alloy 182 weld, the strength is slightly higher and the ductility is lower in the C orientation than in the L orientation.
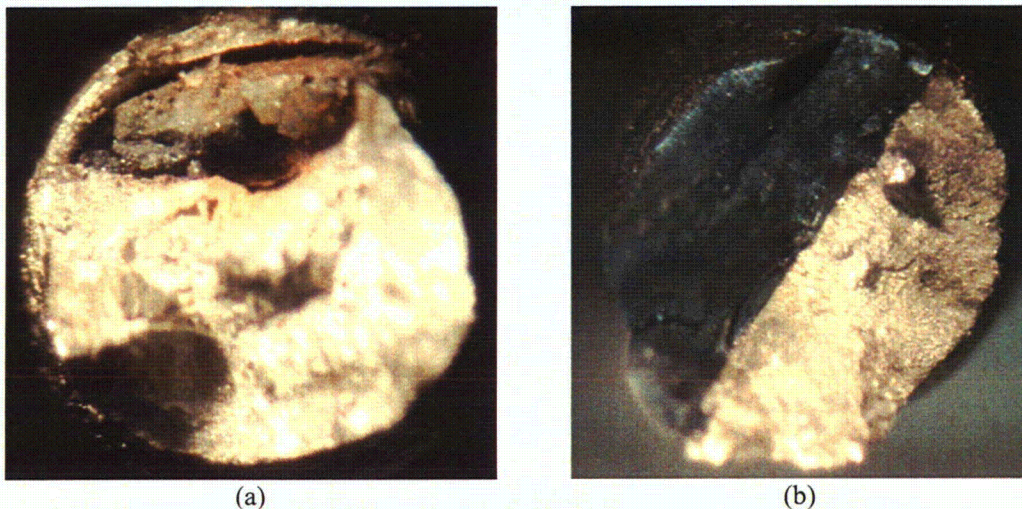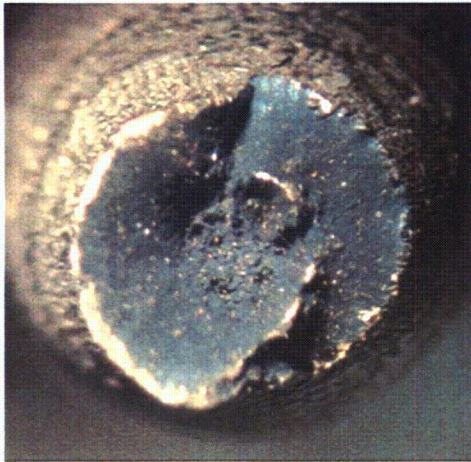

(a)   (b)

Figure 36.   Fracture surfaces of Alloy 182 Specimens (a) J11TL–4, (b) J11TC–1, and (c) J11TC–2 from the Davis-Besse CRDM Nozzle #11 J–groove weld.

Figure 36.   (Contd.)

(c)

4.1.2   Alloys 82 and 182 from the V.C. Summer Nozzle–to–Pipe Weld and Butter

The engineering stress vs. strain curves for Alloy 182 and 82 specimens from the butter and weld regions of the V.C. Summer nozzle–to–pipe dissimilar metal weld are shown in Fig. 37. The values of the yield and of the ultimate stresses and elongation are given in Table 9. The yield and ultimate strengths of Alloy 182 specimens from the butter region of the V.C. Summer weld are higher than those of Alloy 82 specimens from the weld region. This difference in tensile strength may be due to differences in the orientation of the dendritic structure and not to differences in alloy composition. The dendrites are parallel to the stress axis in the weld specimens and transverse to the stress axis for the butter specimens.

Table 9. Tensile test results at 316°C for Alloys 182 and 82 removed from the V.C. Summer nozzle–to–pipe dissimilar metal weld.

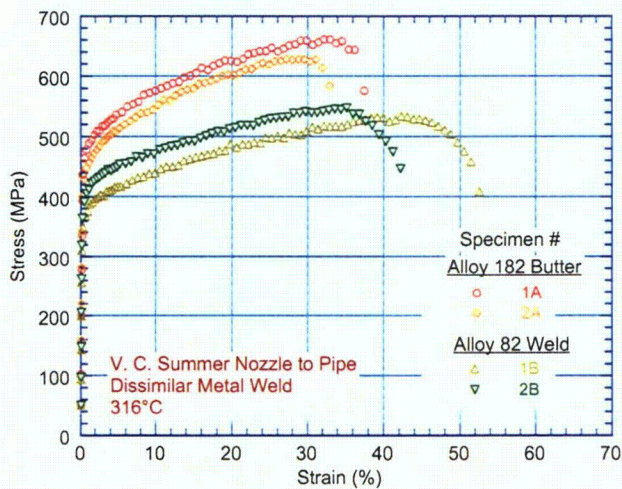| Specimen ID (Alloy Type)	0.2% Yield Stress (MPa)	Ultimate Stress (MPa)	Elongation (%)
WTC-1 (A 82) weld region	320	535	52.6
WTC-2 (A 82) weld region	392	547	42.1
BTC-1 (A 182) butter region	430	662	37.4
BTC-2 (A 182) butter region	424	629	32.9

Figure 37.
Engineering stress vs. strain curves at 316°C for Alloy 182 and 82 specimens from the butter and weld regions of the V.C. Summer nozzle–to–pipe dissimilar metal weld.

35

4.2 Crack Growth Data

4.2.1 Davis–Besse CRDM Nozzle Alloy 600

Crack growth tests have been conducted on 1/4–T CT specimens in L and C orientations (N3CL–1 and N3CC–2, respectively) and 1/2–T CT specimen (N3CC–3) in the C orientation.

4.2.1.1 Specimen N3CL-1

The test conditions, experimental CGRs, the allowed K_{max} from the K/size criterion, and the margin between the applied and allowed K_{max} are given in Table 10. The ECPs of a Pt electrode and a companion Alloy 600 electrode located downstream from the autoclave were –584 and –585 mV, respectively. Fatigue precracking was carried out at $R \approx 0.3$, $K_{max} \approx 20$ MPa·m$^{1/2}$, and triangular waveform with 2–10 Hz frequency. After precracking, R was increased incrementally to 0.5, and the loading waveform was changed to a slow/fast sawtooth with rise time of 30, 300, or 1000 s. The changes in crack length and K_{max} with time during various test periods are shown in Fig. 38. The allowable K_{max}

Table 10. CGR data for 1/4–T CT Specimen N3CL-1 of Alloy 600 in PWR water at 316°C.

Test Period	Test Time (h)	Conductivity (µS/cm)[a]	R Load Ratio	Rise Time (s)	Down Time (s)	Hold Time (s)	Kmax (MPa·m$^{1/2}$)	ΔK (MPa·m$^{1/2}$)	Growth Rate (m/s)	Allowed Kmax (MPa·m$^{1/2}$)	Kapp – Kmax (%)	Crack Length (mm)
Pre a	51	21.0	0.26	1	1	0	20.0	14.8	5.07E-09	20.3	-1	5.993
Pre b	71	–	0.28	5	5	0	19.4	14.0	3.09E-09	20.1	-3	6.117
1	115	–	0.53	30	4	0	21.2	9.9	4.30E-10	19.9	6	6.199
2	194	18.5	0.54	300	4	0	21.5	9.9	2.55E-10	19.9	8	6.240
3a	225	18.5	0.52	300	4	0	22.7	10.9	8.88E-11	19.8	15	6.269
3b	316	14.7	0.51	300	4	0	24.5	12.0	2.63E-10	19.7	25	6.353
4	436	12.8	0.71	300	4	0	25.3	7.3	1.10E-10	19.6	29	6.400
5	676	15.4	0.70	1000	12	0	24.5	7.3	negligible	19.6	25	6.398
6	722	15.4	0.51	300	4	0	25.1	12.3	4.42E-10	19.5	29	6.471
7a	818	13.0	0.50	1000	12	0	24.6	12.3	5.45E-11	19.4	27	6.493
7b	868	13.0	0.51	1000	12	0	25.6	12.5	3.73E-10	19.3	33	6.562

[a]Represents values in the effluent. Feedwater conductivity was about the same as in the effluent. Water flow rate was 50 cc/min.
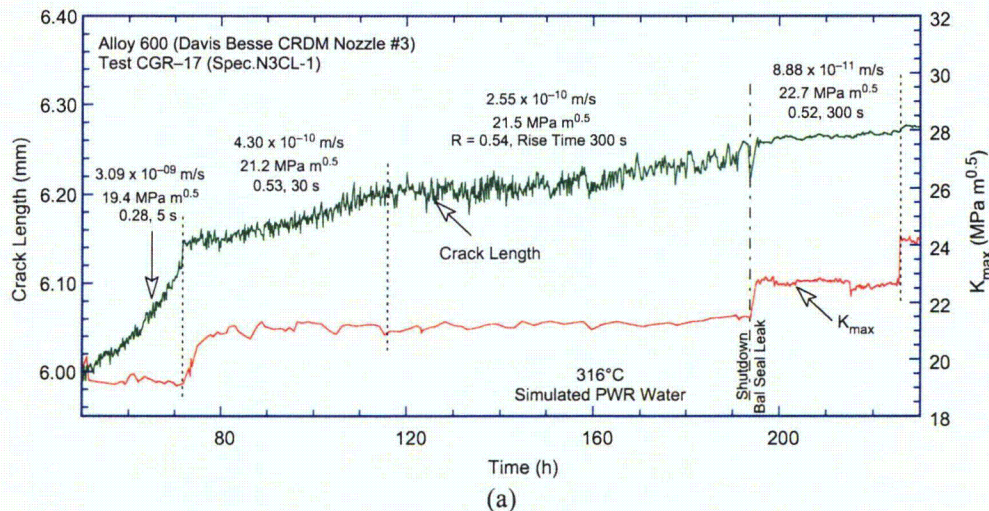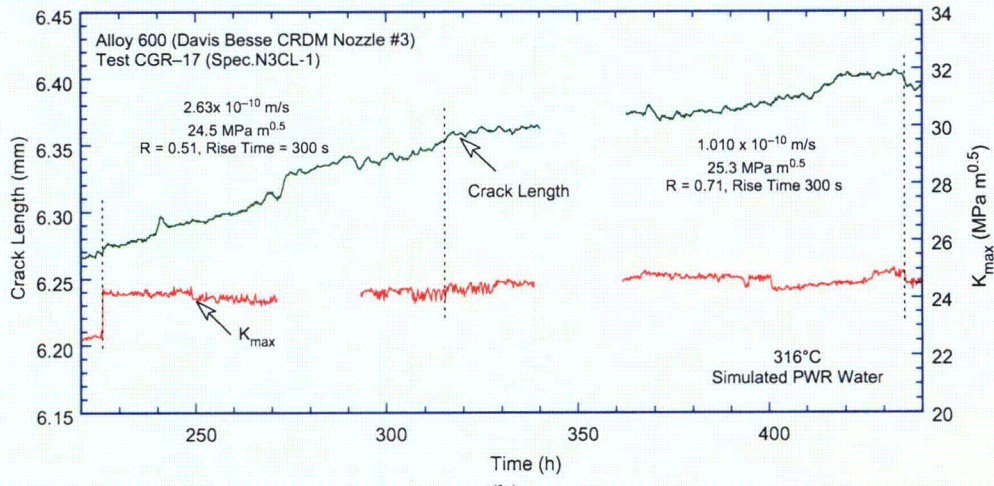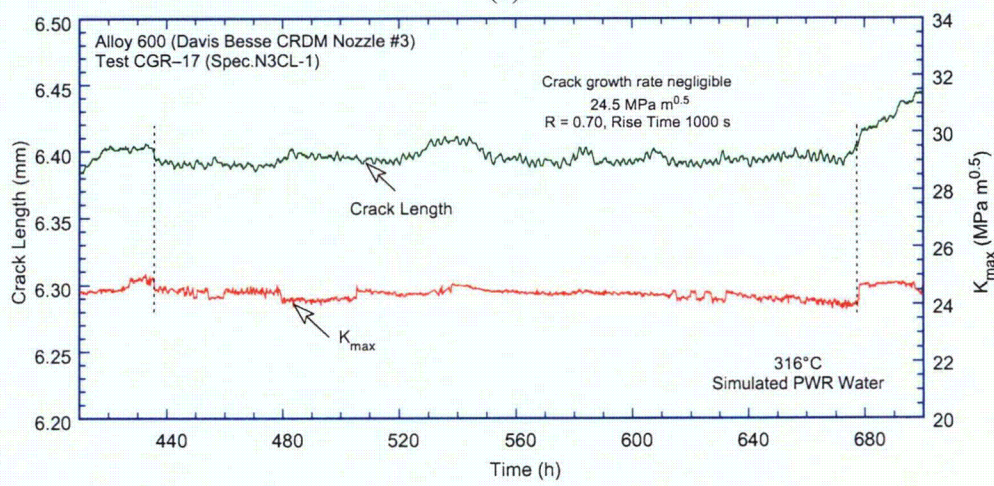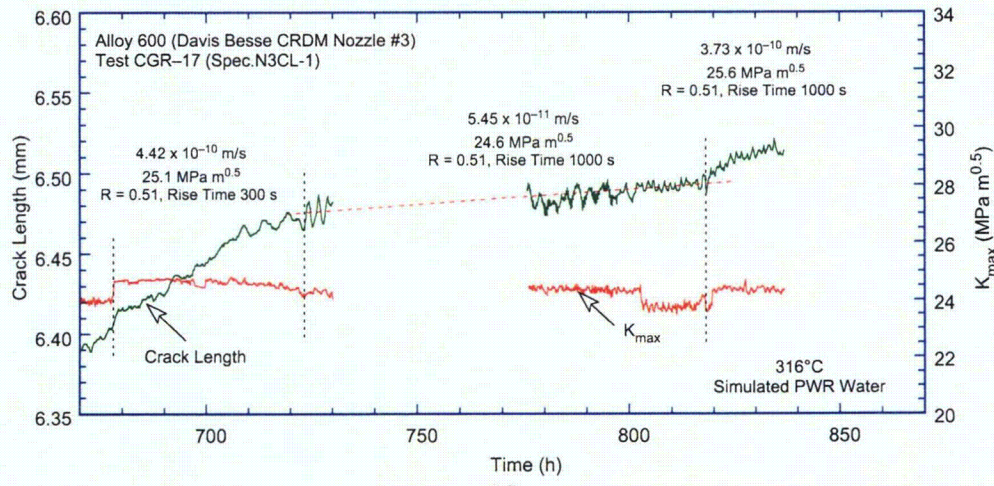

(a)

Figure 38. Crack length vs. time for Specimen N3CL-1 in simulated PWR environment at 320°C during test periods (a) precracking–2, (b) 3–4, (c) 5, and (d) 6–7.

36

(b)

(c)

(d)

Figure 38.   (Contd.)

was calculated from Eq. 12 using flow stress rather than yield stress. For this specimen, the constant–load CGRs were not obtained because at 840 h the CGR increased abruptly by a factor of 5. It was assumed that the applied K_{max} exceeded the value allowed by the K/size criterion, and the test was terminated.

A micrograph covering the entire fracture surface is shown in Fig. 39. The fracture mode was completely IG for all testing periods. The actual crack extension was 83% greater than the value determined from the DC potential drop measurements for this specimen. This difference most likely is due to the presence of secondary cracks and unbroken ligaments on the fracture surface. The crack extensions estimated from the DC potential method were scaled proportionately in both Table 10 and Fig. 38. While for the noncorrected values, the applied K_{max} was within the limits set by the K/size criterion, and the correction resulted in applied K_{max} factors ≈20% larger than maximum allowed by the criterion for most of the test periods.

One unusual feature was the observation of IG fracture very early in the test, e.g., even during precracking (Fig. 39). The fracture mode during precracking at low load ratios and high frequency is generally transgranular (TG). The fracture morphology in the Davis–Besse CRDM nozzle alloy changed from TG to IG when the fatigue crack encountered the very first grain boundary (Figs. 40a and b). In some regions, IG fracture occurred right from the machine notch (Fig. 40a).
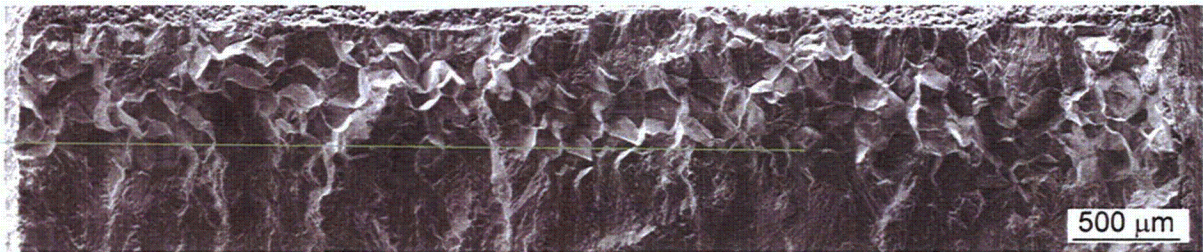

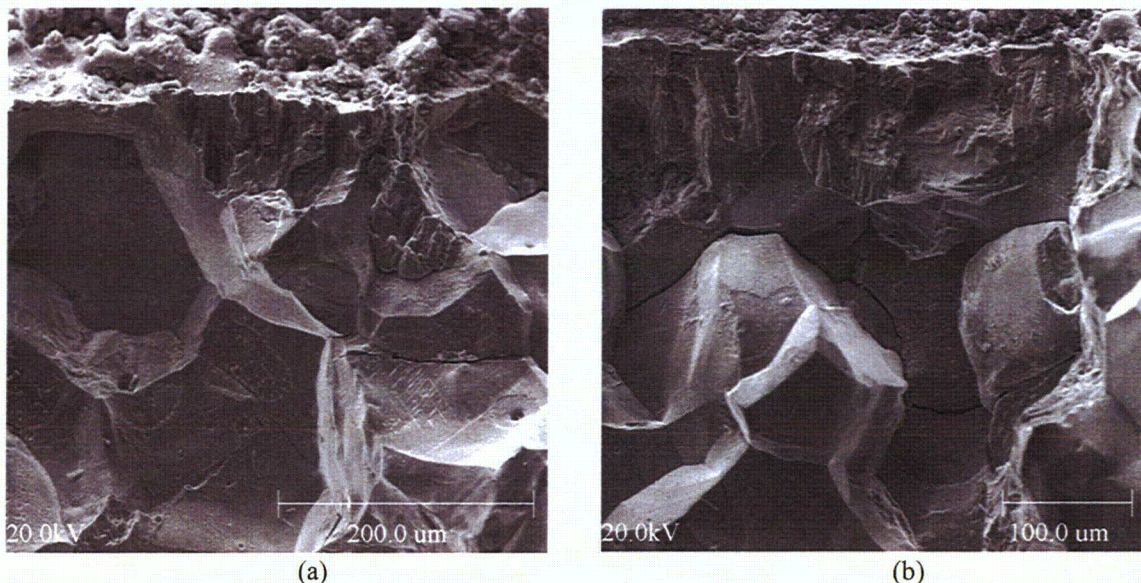Figure 39. Micrograph of the fracture surface of Specimen N3CL–1. Crack advance is from top to bottom.

(a)   (b)

Figure 40. Examples of transition from a TG to an IG fracture mode in Specimen N3CL-1.

4.2.1.2 Specimen N3CC-2

Fatigue precracking was carried out at $R \approx 0.3$, $K_{max} \approx 23$ MPa·m$^{1/2}$, and triangular waveform with 1–0.1 Hz frequency. After ≈ 0.16 mm (6 mil) crack extension, R was increased incrementally to 0.5, and the loading waveform changed to a slow/fast sawtooth with a rise time of 30 or 300 s. The test conditions, experimental CGRs, the allowed K_{max} from K/size criterion, and the margin between the applied and allowed K_{max} are given in Table 11. The changes in crack length and K_{max} with time during various test periods are shown in Fig. 41. For this test, the ECPs of the Pt electrode and the companion Alloy 600 electrode, located downstream from the autoclave, were –706 and –704 mV, respectively. The test was interrupted at ≈ 1220 h because of a leak. The test was restarted at $R \approx 0.5$, $K_{max} \approx 24.5$ MPa·m$^{1/2}$, and a slow/fast sawtooth waveform with a 300-s rise time.

Table 11. CGR data for 1/4–T CT Specimen N3CC-2 of Alloy 600 in PWR water at 316°C.

Test Period	Test Time (h)	Conduc- tivity[a] (μS/cm)	R Load Ratio	Rise Time (s)	Down Time (s)	Hold Time (s)	Kmax (MPa·m$^{1/2}$)	ΔK (MPa·m$^{1/2}$)	Growth Rate (m/s)	Allowed Kmax (MPa·m$^{1/2}$)	K_{app} – Kmax (%)	Crack Length (mm)
Pre a	189	22	0.31	5	5	0	23.1	15.9	7.52E-10	19.9	16	6.243
1	383	20	0.51	300	4	0	22.3	10.9	2.13E-11	19.8	12	6.270
2	457	17	0.51	30	4	0	22.9	11.2	6.05E-11	19.7	16	6.335
3	550	16	0.51	300	4	0	22.8	11.2	9.46E-12	19.7	16	6.338
4	580	15	0.51	30	4	0	24.9	12.2	8.59E-10	19.6	27	6.415
5	765	15	0.50	300	12	0	24.8	12.4	8.87E-11	19.5	28	6.471
6	885	15	0.70	300	12	0	25.0	7.5	5.28E-11	19.4	29	6.492
7	912	16	0.51	300	12	0	25.1	12.3	1.01E-10	19.4	29	6.502
8	1197	20	0.52	300	12	3600	25.7	12.4	6.92E-11	19.3	33	6.541
9	1365	21	0.48	300	12	0	24.6	12.8	7.53E-11	19.2	28	6.617
10	1530	21	1.00	–	–	–	24.7	–	9.67E-11	19.1	29	6.658

[a]Represents values in the effluent. Feedwater conductivity was about the same as in the effluent. Water flow rate was 42 cc/min.

The fracture surface of Specimen N3CC–2 is shown in Fig. 42. As in the previous test, the fracture mode was completely IG for all test periods; the fracture started as TG but changed to IG almost at the first grain boundary encountered. A slice of the entire crack extension is shown in Fig. 43a, and typical fracture morphology at select locations on the surface is shown in Figs. 43b and c. The precrack area at location A shows TG fracture only up to the nearest grain boundary, and location B shows smooth IG
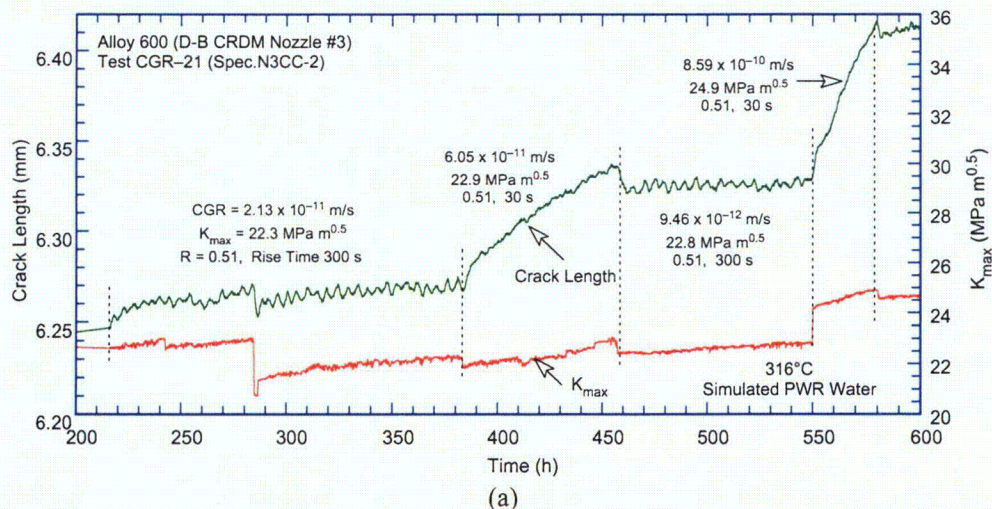

(a)

Figure 41. Crack length vs. time for Specimen N3CC-2 in a simulated PWR environment at 320°C during test periods (a) 1–4, (b) 5–8, and (c) 10–11.
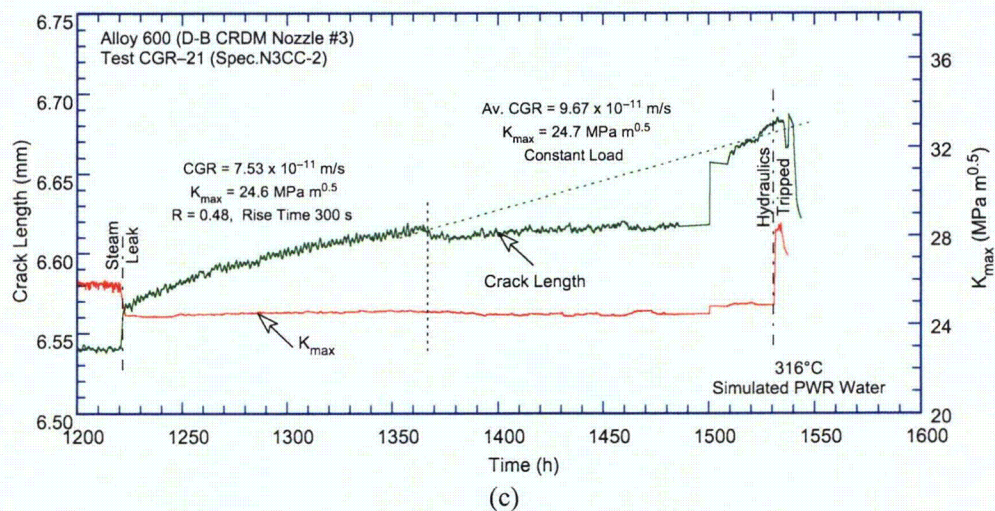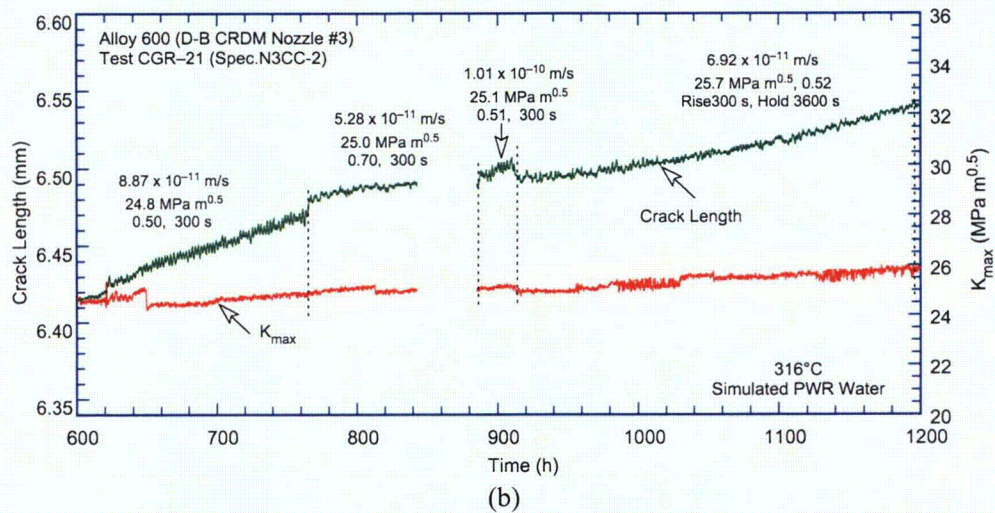
39

Figure 41. (Contd.)

fracture. The Ti–rich precipitates on the surface in Fig. 43c do not seem to affect the fracture mode. While the focus of this study was not on the effect of the Ti carbides on the SCC behavior of the alloy at hand, these particles can have a negative impact. As such, the precipitation of Ti carbides can reduce the concentration of free carbon retained in the matrix to a level at which it limits the precipitation of the desirable grain boundary chromium carbides. In addition, if Ti carbides precipitate at grain boundaries, they oxidize when exposed to the high–temperature water environment, possibly leading to grain boundary embrittlement.

The actual crack extension was 74% greater than the value determined from the DC potential drop method. Crack extensions estimated from the DC potential method were scaled proportionately; the corrected values of K_{max} and growth rate are given in Table 11. The results in Tables 10 and 11 indicate that for Specimens N3CL–1 and N3CC–2, the applied K_{max} for most of the test periods was $\approx$20% higher than the value allowed by the K/size criterion.
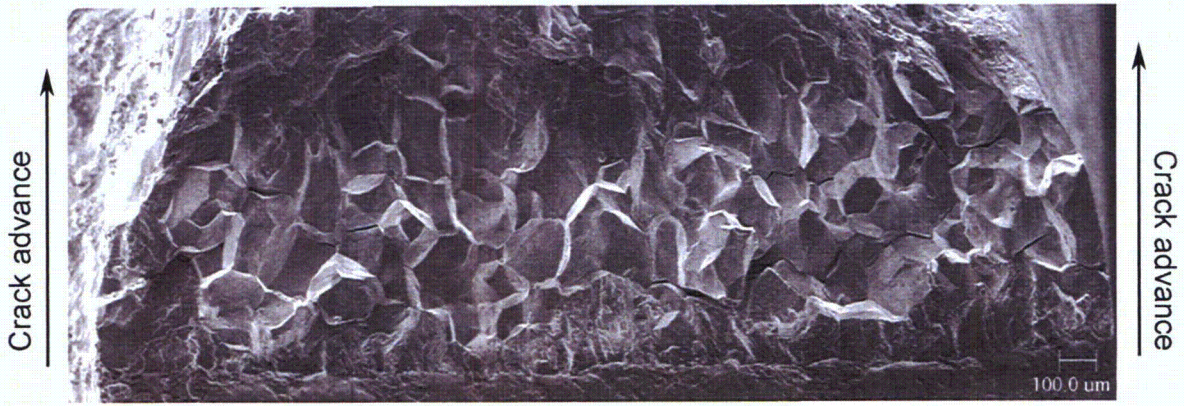
40

Figure 42. Micrograph of the fracture surface of Specimen N3CC–2. Crack advance is from bottom to top.
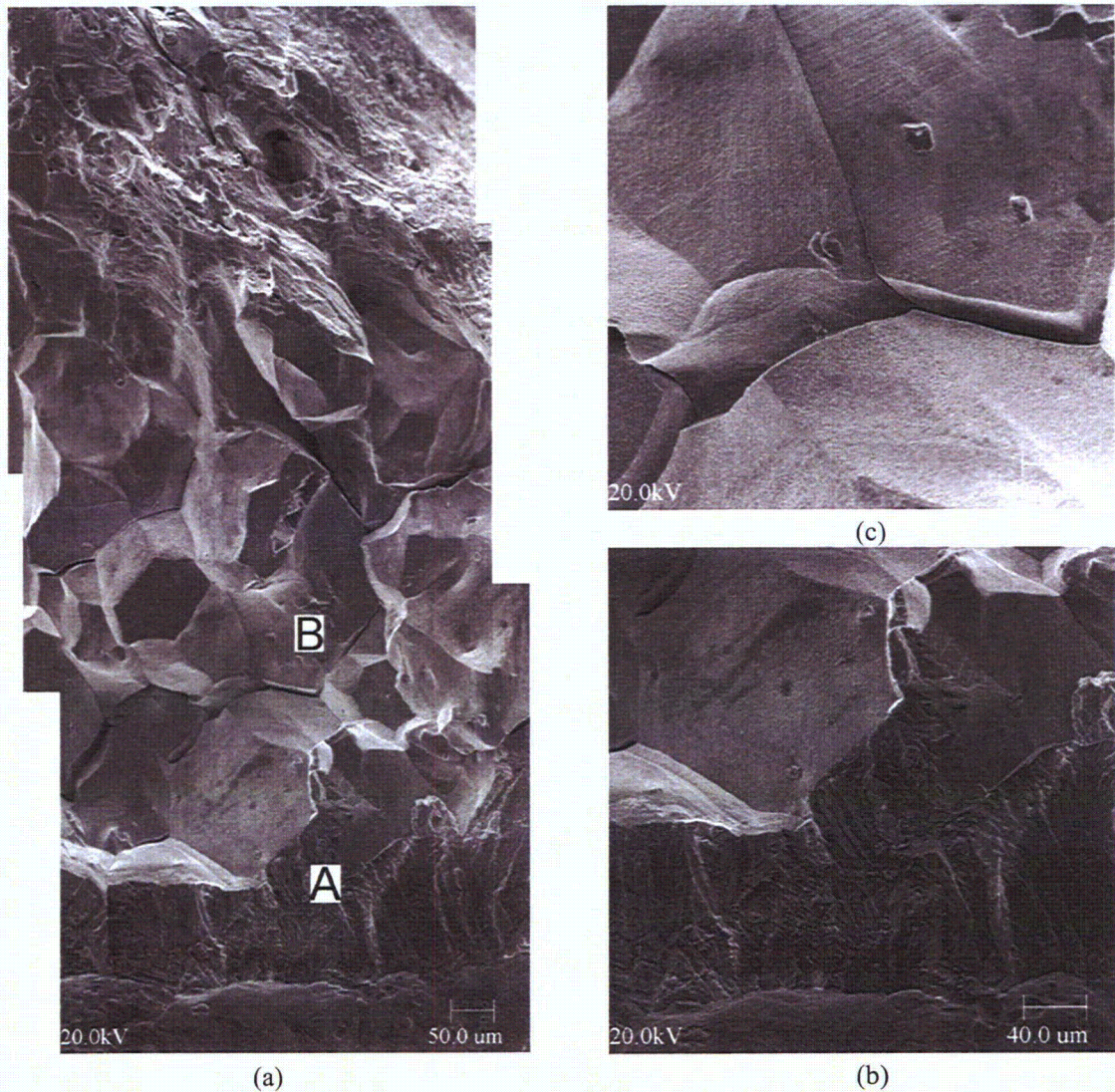

(a)

(b)

(c)

Figure 43. (a) Fracture surface of Specimen N3CC-2 and high-magnification micrographs at locations (b) A and (c) B.

4.2.1.3 Specimen N3CC-3

Testing for this specimen was carried out in a fashion similar to that of the previous two Alloy 600 specimens from Davis-Besse. However, unlike the previous two specimens, N3CC-3 was a 1/2–T CT specimen. Fatigue precracking was carried out at $R \approx 0.3$, $K_{max} \approx 20$ MPa·m$^{1/2}$, triangular waveform, and frequency of 2 or 0.1 Hz. After an ≈ 0.3– (12–mil) crack extension, R was increased incrementally to 0.5, and the loading waveform changed to a slow/fast sawtooth with rise time of 60 or 300 s. The test was interrupted at ≈ 530 h when the strain limit tripped the test, causing the specimen to overstrain. The test was restarted under the loading conditions prior to the interruption. However, no crack growth was observed even after 120 h, and the test was terminated. The changes in crack length and K_{max} with time are given in Table 12 and plotted in Fig. 44. The ECPs of the Pt electrode and the companion Alloy 600 electrode, located downstream from the autoclave, were –565 and –563 mV, respectively.

Table 12. CGR data for Specimen N3CC-3 in PWR water[a] at 316°C.

Test Period	Test Time (h)	Conduc- tivity[b] (μS/cm)	R Load Ratio	Rise Time (s)	Down Time (s)	Hold Time (s)	Kmax (MPa·m$^{1/2}$)	ΔK (MPa·m$^{1/2}$)	Growth Rate (m/s)	Allowed Kmax (MPa·m$^{1/2}$)	K_{app} – Kmax[c] (%)	Crack Length (mm)
Pre a	50	20	0.36	0.25	0.25	0	20.8	13.3	1.35E-08	27.6	-25	12.777
Pre b	55	20	0.35	0.25	0.25	0	20.2	13.1	8.41E-09	27.5	-26	12.872
Pre c	72	19	0.33	5.0	5.0	0	19.9	13.3	2.03E-09	27.4	-27	12.943
Pre d	78	19	0.32	0.5	0.5	0	20.7	14.1	1.31E-08	27.2	-24	13.065
1	97	18	0.50	12	4	0	20.6	10.3	9.08E-10	27.1	-24	13.157
2	122	18	0.49	60	4	0	20.8	10.6	3.55E-10	27.1	-23	13.186
3	147	18	0.48	300	4	0	20.9	10.9	2.80E-10	27.1	-23	13.206
4	174	17	0.63	1,000	12	0	21.2	7.8	2.18E-10	27.0	-22	13.249
5a	230	16	1.00	-	-	-	20.5	0.00	7.85E-11	27.1	-24	13.218
5b	339	15	1.00	-	-	-	20.9	0.00	1.25E-10	26.9	-22	13.319
6a	386	14	1.00	-	-	-	26.4	0.00	2.28E-10	26.8	-2	13.404
6b	529	12	1.00	-	-	-	26.7	0.00	1.55E-10	26.7	0	13.510
7	648	12	1.00	-	-	-	31.9	0.00	negligible	26.5	20	13.637

[a]Simulated PWR water with 2 ppm Li, 1000 ppm B, and ≈ 2 ppm dissolved hydrogen. Effluent DO was <10 ppb.
[b]Represents values in the effluent.
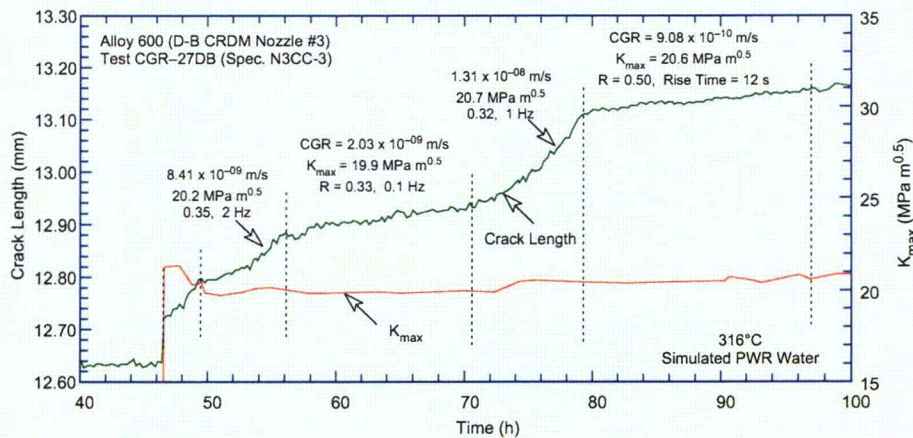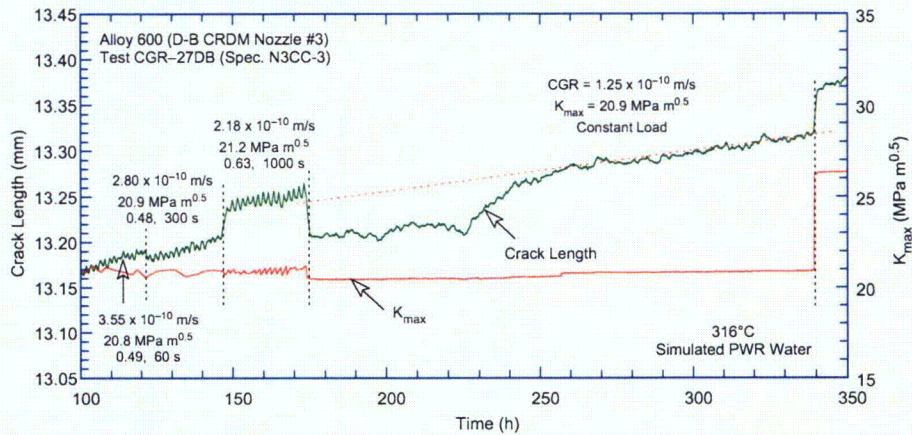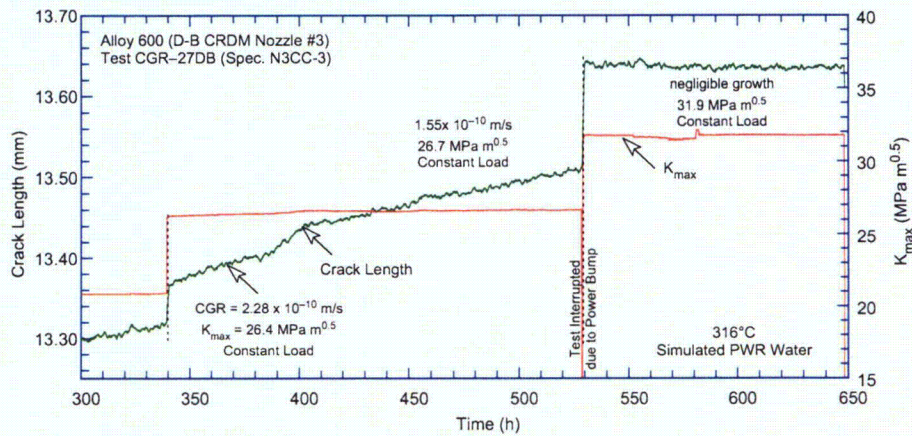[c]Based on flow stress.

(a)

Figure 44. Crack length vs. time plots for Specimen N3CC-3 of Alloy 182 in PWR water at 316°C during test periods (a) precracking–1, (b) 2–5, and (c) 6–7.

(b)

(c)

Figure 44. (Contd.)

After the test, the final crack size was marked by fatigue cycling in air at room temperature. The specimen was then fractured, and the fracture surface was examined in the SEM. Figure 45 shows the entire fracture surface. The beginning of the IG region is shown with green, and the end of the test is shown with red. Also shown, with yellow, are regions of smooth IG fracture in the initial TG region. The final crack advance was measured from the SEM micrograph in Fig. 45. The actual crack length was ≈57% greater than the value determined from the DC potential measurements. The experimental crack extensions were scaled proportionately. The corrected test results, allowed K_{max} from K/size values, and the margins between the applied and allowed K_{max} are given in Table 12 and Fig. 44. In this test, the allowed K_{max} was not exceeded.
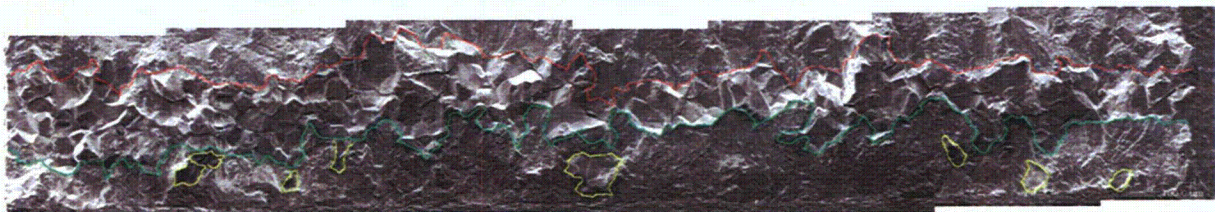

Figure 45. Micrograph of the fracture surface of Specimen N3CC–3. Crack growth is from bottom to top.

Unlike the previous two specimens where an IG fracture mode was observed right from the beginning, this specimen exhibited a TG region at the start of the test; that is, under more rapid cyclic loading, the crack growth is dominated by mechanical fatigue. The CGRs during precracking and initial periods of cyclic loading were primarily due to mechanical fatigue. For the present test, environmental enhancement typically was observed at load ratios $R \geq 0.5$ and rise times ≥ 30 s.

To better illustrate these features, Fig. 46 shows a portion of the fracture surface of the specimen at higher magnification. Figure 46a shows the full extent of the crack, from the machined notch (bottom of the picture) to the end of the test. During precracking, the crack advances in a predominantly TG mode; however, grains appear well–defined and IG cracks are also observed. Moreover, as already indicated, several locations are characterized by smooth IG fracture (indicated by white arrows in

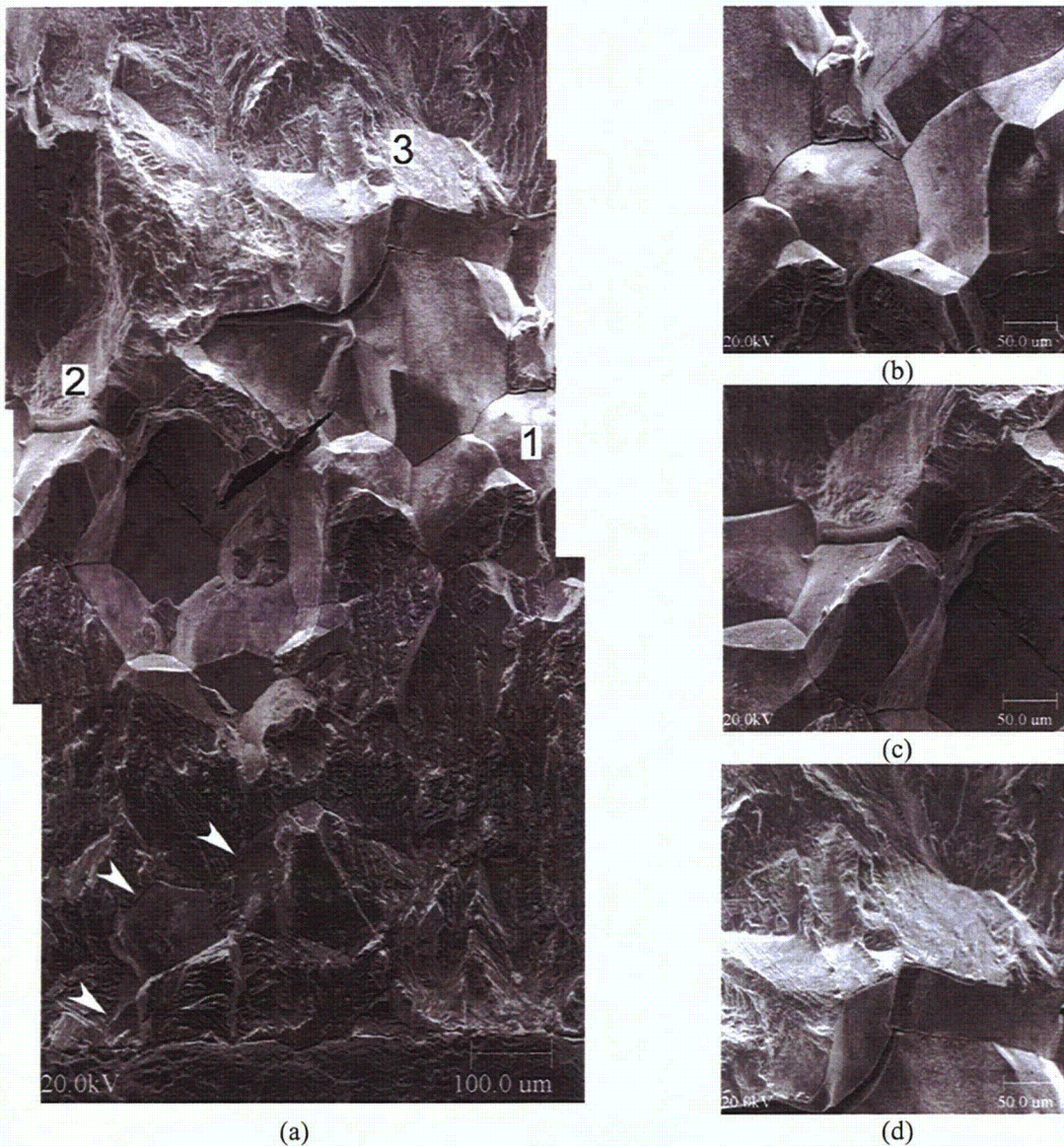(a)   (d)

Figure 46. (a) Micrograph showing a portion of the fracture surface of N3CC-3 and high-magnification micrographs at locations (b) 1, (c) 2, and (d) 3. The arrows indicate grains exhibiting smooth IG in the TG region corresponding to the precracking periods.

Fig. 46a). As with the previous specimens, smooth IG fracture was observed right from the beginning of the test in regions corresponding to fatigue cracking. Several high–magnification micrographs taken at locations 1–3 are shown in Figs. 46b–d. Figure 46b (location 1 in Fig. 46a) shows an example of smooth IG fracture from the exclusively IG region corresponding to the constant–load test period. Figure 46c (location 2 in Fig. 46a) shows the fracture surface in a region near the end of the test, and Fig. 46d (location 3 in Fig. 46a) is a micrograph showing the area at the end of the test. One interesting feature of Fig. 46c is that while the last two boundaries encountered by the propagating SCC crack are well-defined, thus likely to crack, the crack follows a TG path in close proximity to the boundary, but not along the boundary.

4.2.2 Davis–Besse J–Groove Weld

Crack growth tests have been conducted on 1/4–T and 1/2–T CT specimens in C orientation (Specimens J11CC–1 and J11CC–3, respectively).

4.2.2.1 Specimen J11CC-1

Fatigue precracking was carried out at $R \approx 0.3$, $K_{max} \approx 20.0$ MPa·m$^{1/2}$, and triangular waveform with 1–0.01 Hz frequency. After ≈ 0.18-mm (7 mil) crack extension, R was increased incrementally to 0.7, and the loading waveform changed to a slow/fast sawtooth with rise time of 300 s or 1000 s. The ECPs of the Pt electrode and the companion Alloy 600 electrode located downstream from the autoclave were –648 and –651 mV, respectively. The test conditions, experimental CGRs, the allowed K_{max} from K/size criterion, and the margin between the applied and allowed K_{max} are given in Table 13. The changes in crack length and K_{max} with time during test periods 3–13 are shown in Fig. 47.

Table 13. CGR data for Specimen J11CC-1 of Alloy 182 J–groove weld in PWR water[a] at 316°C.

Test Period	Test Time (h)	Conduc-tivity[b] (μS/cm)	R Load Ratio	Rise Time (s)	Down Time (s)	Hold Time (s)	Kmax (MPa·m$^{1/2}$)	ΔK (MPa·m$^{1/2}$)	Growth Rate, (m/s)	Allowed Kmax[c] (MPa·m$^{1/2}$)	Kapp – Kmax[c] (%)	Crack Length (mm)
Pre a	145	17.2	0.30	0.5	0.5	0	22.5	15.7	4.05E-08	20.9	8	6.153
Pre b	186	17.2	0.31	50	50	0	21.8	15.1	1.27E-09	20.7	5	6.264
1	331	15.6	0.50	300	4	0	21.8	10.9	1.13E-10	20.5	6	6.333
2	453	13.0	0.70	1000	12	0	22.6	6.8	5.71E-12	20.5	10	6.342
3a	644	22.2	0.49	1000	12	0	22.4	11.4	3.88E-11	20.5	9	6.363
3b	745	20.0	0.49	1000	12	0	22.3	11.4	negligible	20.4	9	6.382
4	937	14.7	0.49	1000	12	0	23.8	12.2	8.25E-12	20.4	17	6.392
5	987	14.7	0.49	300	12	0	23.8	12.2	5.53E-11	20.4	17	6.401
6	1106	18.2	0.49	300	12	3600	23.9	12.2	negligible	20.4	17	6.402
7	1178	18.9	0.51	30	4	0	24.2	11.9	7.93E-10	20.4	20	6.525
8	1248	17.2	0.48	300	12	0	24.3	12.6	1.06E-10	20.4	21	6.550
9	1415	16.1	0.74	300	12	3600	24.3	6.4	negligible	20.4	20	6.543
10	1443	18.2	0.48	30	12	0	24.6	12.9	1.13E-09	20.0	23	6.616
11	1513	18.5	0.48	300	12	0	29.0	15.0	3.00E-10	19.8	47	6.742
12	1548	18.5	0.48	300	12	3600	29.3	15.1	4.00E-11[d]	19.8	48	6.747
13	1948	16.7	1.0	–	–	–	30.3	0.0	1.63E-11[e]	19.7	54	6.797

[a]Simulated PWR water with 2 ppm Li, 1000 ppm B, and ≈2 ppm dissolved hydrogen (23 cc/kg).
[b]Represents values in the effluent. Feedwater conductivity was about the same as in the effluent. Effluent DO was <10 ppb.
[c]Based on flow stress.
[d]From superposition model, CGR during the constant load was estimated to be 1.68E-11 m/s.
[e]Based on total crack extension during the period.

For this specimen, relatively high CGRs were observed under cyclic loading (e.g., $>1 \times 10^{-10}$ m/s), but attempts to transition to constant load by increasing the load ratio and/or rise time, decreased the CGRs to very low levels. As shown in Table 13, during test period 2, the CGR decreased markedly at R = 0.7 and a rise time of 1000 s. The CGR also decreased significantly each time a 3600–h hold period

was added to the cycle, e.g., during test periods 6, 9, and 12. Measurable growth rates were observed when K_{max} was increased above 25 MPa·m$^{1/2}$ and at R = 0.5 and a 300 s rise time. The CGR under the final constant–load test period at $K_{max} \approx 30$ MPa·m$^{1/2}$ was relatively low.
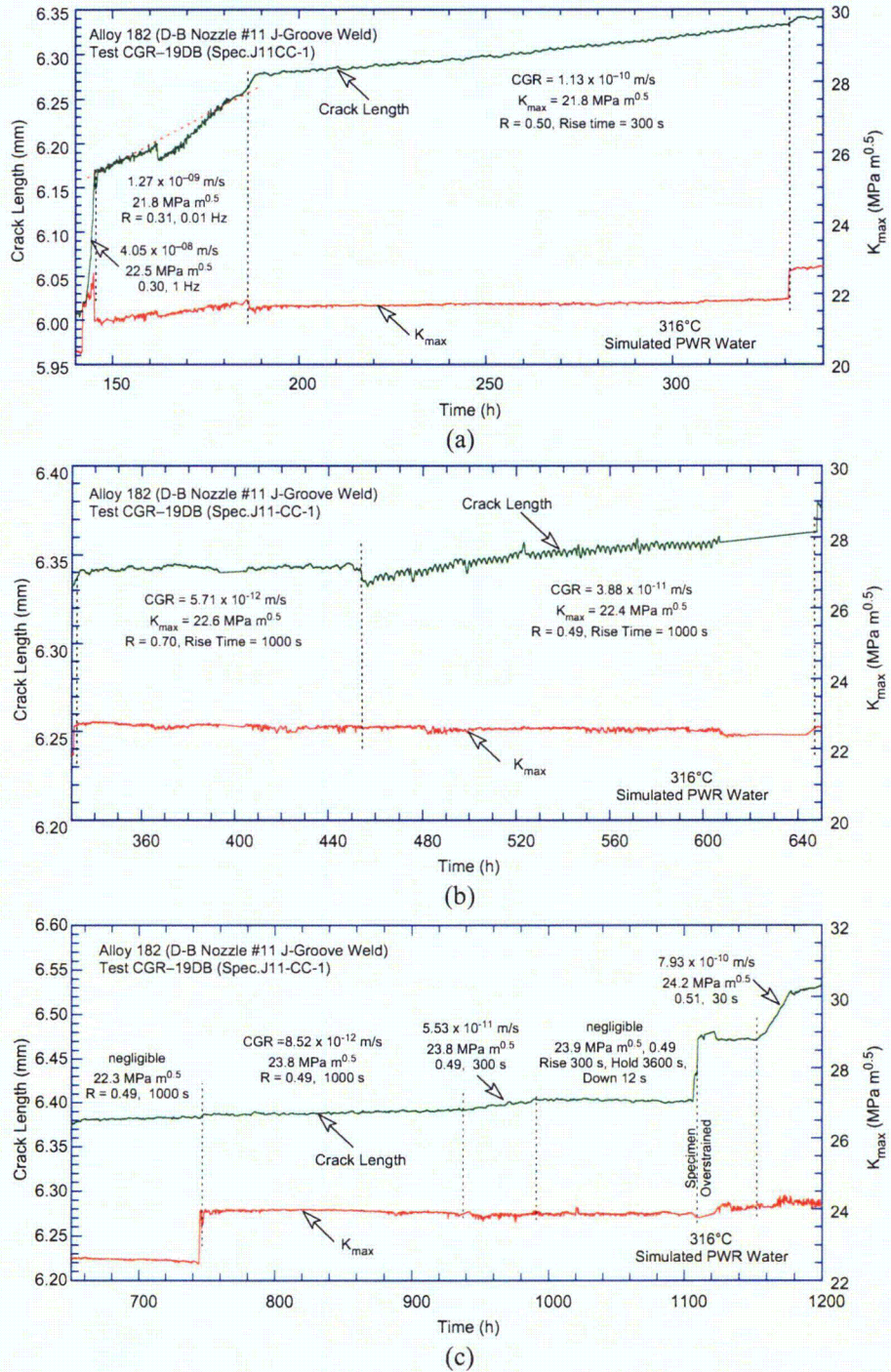

Figure 47. Crack length vs. time plots for Specimen J11CC-1 of Alloy 182 J–groove weld in PWR water at 316°C during test periods (a) precracking, (b) 1–3a, (c) 3b–7, (d) 8–11, and (e) 12–13.
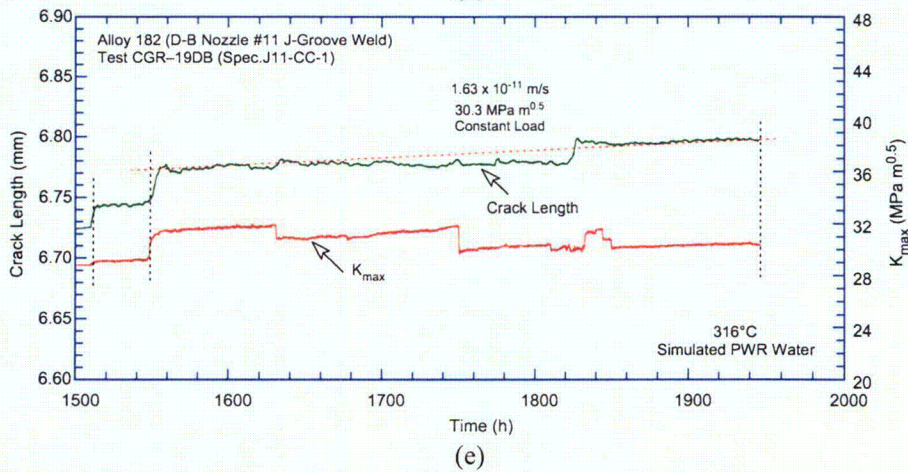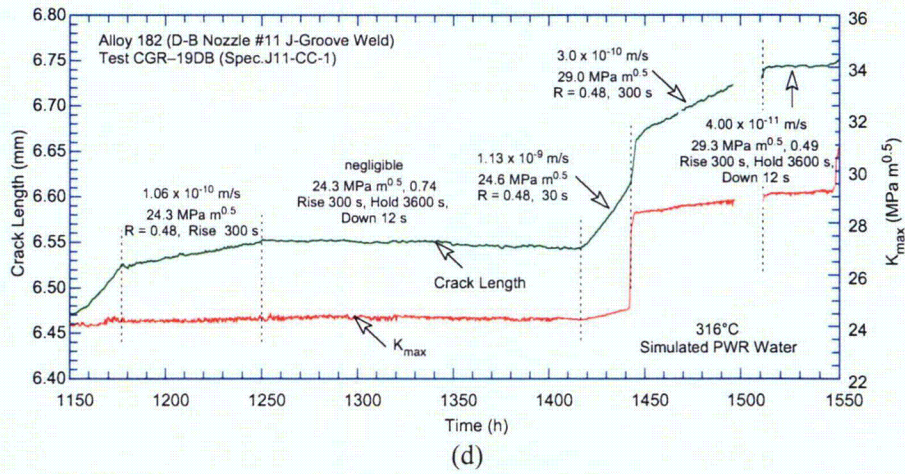
(d)

(e)

Figure 47.   (Contd.)

Figure 48 shows the entire crack extension for the specimen. On the basis of this photograph, the actual crack extension was estimated to be 60% greater than the value determined from the DC potential drop method; the values shown in Table 13 and Fig. 47 have been corrected accordingly.

Figure 48.   Crack front on Sample J11CC-1. Crack growth is from top to bottom.

Figure 48 shows that after precracking, the fracture turned into a mixed transgranular and IG fracture mode. While it appears that TG fracture is the dominant mode overall, the area near the left edge contains more IG fracture than the average. The crack also appears to be pinned on the left side on the photo, most likely by a material defect. Furthermore, the appearance of the crack front suggests that pinning occurred throughout the fracture surface, thereby impeding the crack advance. Several locations where pinning was evident are indicated by arrows in Fig. 48.

47

A detailed examination at high magnification was conducted at three locations on the fracture surface, designated by A, B, and C in Fig. 48. Figure 49 shows an example of crack morphology at position A. Figures 49a and 49b are examples of mixed TG and IG fracture. The secondary cracks visible in Fig. 49b are consistent with an IG fracture mode. Figure 49c is a high-magnification micrograph taken at what appears to be a pinning point. The presence of striations (top center) suggests a TG fracture mode. These two observations suggest that the SCC-driven, IG-propagating crack was stopped at obstacles. The crack front apparently overcame the obstacles only after the loading conditions were changed to promote mechanical fatigue.
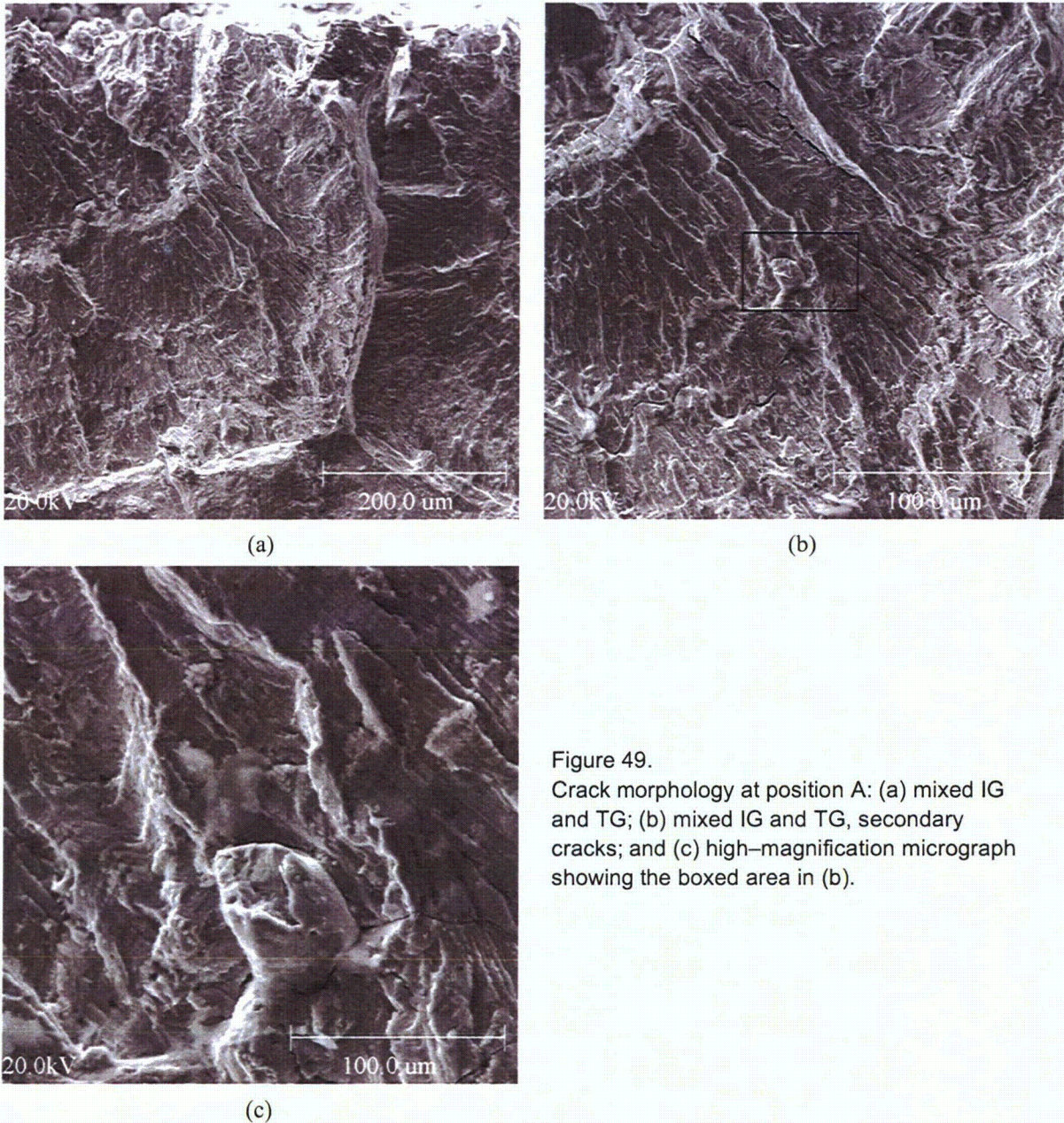

(a)

(b)

(c)

Figure 49.
Crack morphology at position A: (a) mixed IG and TG; (b) mixed IG and TG, secondary cracks; and (c) high–magnification micrograph showing the boxed area in (b).

48

Figure 50 shows the crack morphology at position B in Fig 48. Figures 50a and b are examples of mixed IG and TG, and Figs. 50c and d are high–magnification micrographs at locations indicated by arrows in Fig. 50a. The upper right-hand corner of Fig. 50c shows a relatively smooth surface, while Fig. 50d shows rounded shapes typical of dendritic undulations, both cases typical of SCC-driven crack advance. The crack growth was apparently interrupted by pinning points, two of which are visible in Fig. 50c. Out–of–plane cracks are also apparent in Figs. 50c and d. While these may be preexisting cracks, none were observed during metallography. More likely, they formed during the test at either the advancing crack tip or after the crack tip has passed. Since these cracks seem to follow the pinning pattern of the fracture surface, the first hypothesis – crack branching at the crack tip – seems more probable. The root cause for the occurrence of these cracks is unknown.
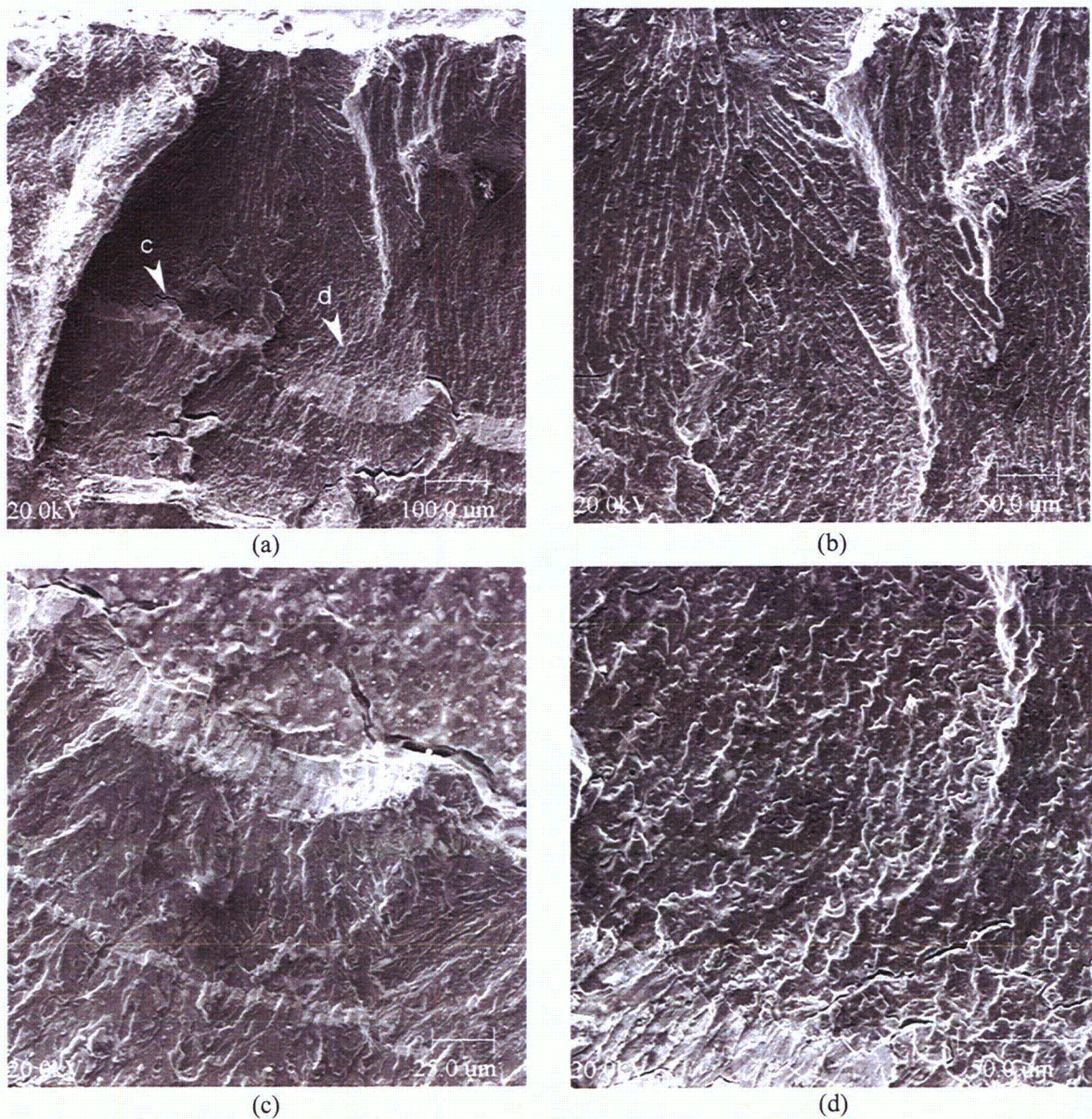

(a)

(b)

(c)

(d)

Figure 50. Crack morphology at position B: (a, b) mixed IG and TG, and (c, d) high-magnification micrographs at locations indicated by arrows in (a).

Figure 51 further substantiates the observations just made. Figure 51a shows the crack morphology at position C in Fig 48. Figure 51b shows a mixed IG/TG mode. The striations on the fracture surface past the pinning point, Fig. 51c, seem to indicate that the SCC-driven crack was pinned and unable to advance unless fatigue driven. Out–of–plane cracks were also observed, as indicated in Fig. 51b.
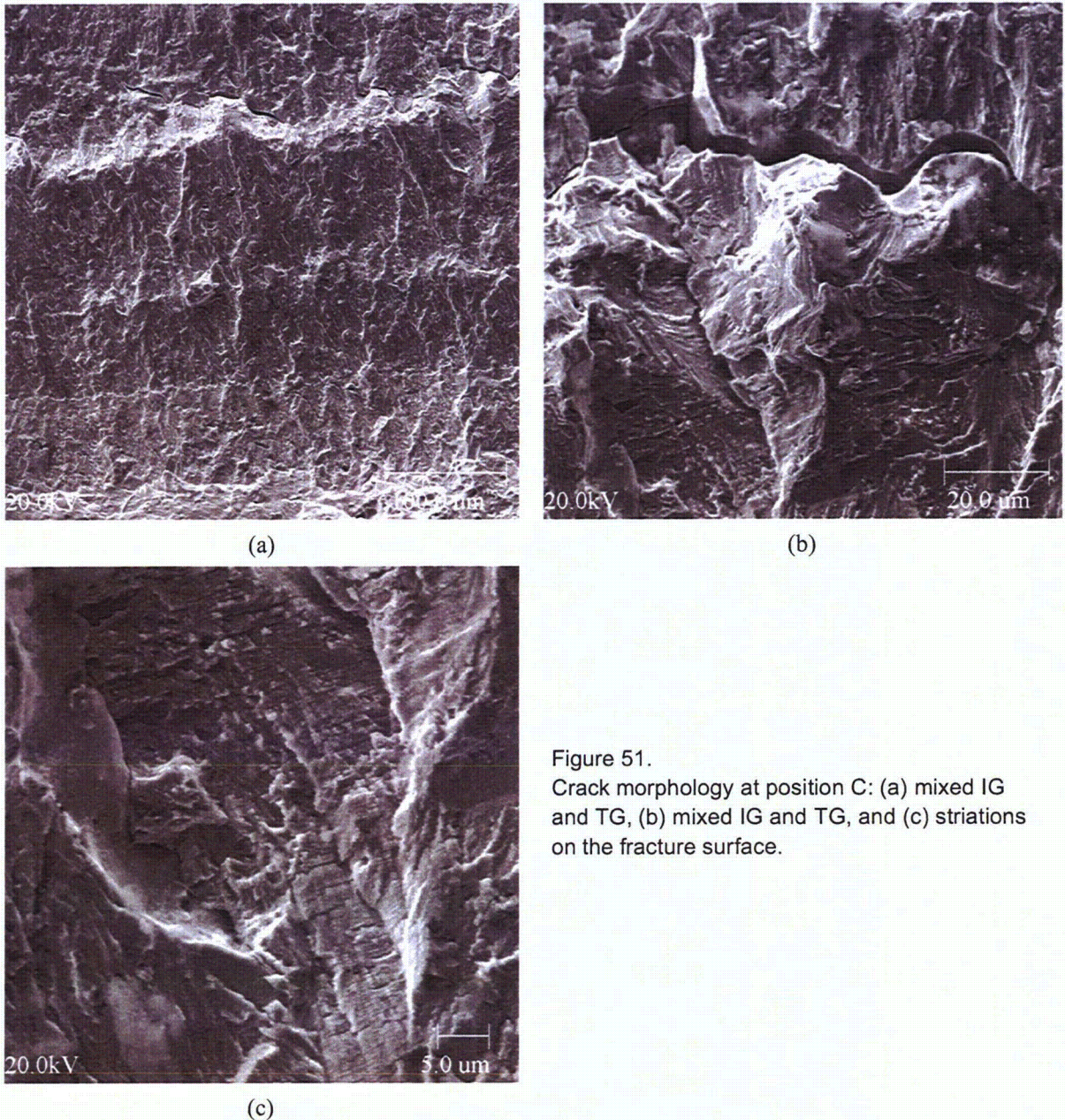

(a)

(b)

(c)

Figure 51.
Crack morphology at position C: (a) mixed IG and TG, (b) mixed IG and TG, and (c) striations on the fracture surface.

4.2.2.2 Specimen J11CC-3

Testing for this specimen was similar to that of the previous Alloy 182 specimen from the Davis–Besse CRDM nozzle J–groove weld. However, Specimen J11CC-3 was a 1/2–T CT specimen. Fatigue precracking was carried out at $R \approx 0.3$, $K_{max} \approx 18.0$ MPa·m$^{1/2}$, and triangular waveform with 0.5–0.01 Hz

frequency. Next, R was increased incrementally to 0.7, and the loading waveform changed to a slow/fast sawtooth with rise time of 300 s or 1000 s. The test conditions, experimental CGRs, the allowed K_{max} from K/size criterion, and the margin between the applied and allowed K_{max} are given in Table 14. The changes in crack length and K_{max} with time are shown in Fig. 52.

A significant result for this specimen is the very low CGRs under constant load, with or without periodic partial unloading. Also, every time the loading was changed from a sawtooth waveform to constant load, the crack length estimated from the DC potential measurements decreased by ≈20 μm, as indicated by Fig. 52. Our experience to date has been that the DC potential drop method measures crack length accurately when the fracture morphology is TG, but when the fracture mode is IG, the potential drop underestimated the actual crack length, most likely because of the presence of unbroken ligaments or secondary cracks. In an attempt to obtain more consistent crack-length measurements by DC potential drop, the specimen was subjected to short periods of cyclic loading with a sawtooth waveform at R = 0.5 or 0.7 and a 300– or 1000–s rise time before and after each constant load test period, e.g., test periods 7, 9, and 13. The average crack length during these short test periods was used to determine the CGRs for the constant–load test periods; the values are given in Table 14.

Table 14. CGR data for Specimen J11CC-3 in PWR water[a] at 316°C.

| Test Period	Test Time (h)	Conduc- tivity[b] (μS/cm)	R Load Ratio	Rise Time (s)	Down Time (s)	Hold Time (s)	K_{max} (MPa·m$^{1/2}$)	ΔK (MPa·m$^{1/2}$)	Growth Rate (m/s)	Allowed K_{max} (MPa·m$^{1/2}$)	K_{app} – K_{max}[c] (%)	Crack Length (mm)
Pre a	78	21	0.31	0.25	0.25	0	18.78	13.17	6.55E-08	29.40	-36	12.373
Pre b	104	21	0.32	10	10	0	18.96	13.02	7.17E-09	29.10	-35	12.605
1	221	18	0.50	60	4	0	19.81	9.94	7.44E-10	28.53	-31	13.049
2	412	20	0.51	300	12	0	19.95	9.97	1.33E-10	28.42	-30	13.134
3	507	20	1.00	–	–	–	19.99	0.00	3.92E-11[d]	28.47	-30	13.157
4	580	19	0.50	300	12	0	22.08	11.10	2.30E-10	28.29	-22	13.233
5	742	15	0.50	1000	12	0	22.21	11.13	7.12E-11	28.27	-21	13.254
6a	864	13	1.00	–	–	–	22.23	0.00	–	28.33	-22	13.246
6b	934	13	0.51	12	12	3600	22.16	11.07	3.93E-11[d]	28.33	-22	13.282
7b	941	19	0.70	1000	12	0	28.11	8.45	–	28.21	0	–
8	1079	33	0.70	12	12	3600	28.18	8.46	4.00E-11	28.24	0	13.271
9	1084	33	0.70	1000	12	0	28.36	14.41	–	28.19	1	13.312
10	1248	31	0.70	12	12	3600	32.72	9.82	4.65E-11	28.17	16	13.327
11	1349	29	0.69	1000	12	0	32.80	10.04	8.23E-11	28.06	17	13.410
12	1516	28	0.70	12	12	3600	32.60	9.78	negligible	28.12	16	13.368
13	1537	28	0.70	300	12	0	32.74	9.82	–	28.07	17	13.405

[a]Simulated PWR water with 2 ppm Li, 1000 ppm B, and ≈2 ppm dissolved hydrogen. Effluent DO was <10 ppb.
[b]Represents values in the effluent; ECP measurements were not made because of problems with the reference electrode. Feedwater conductivity was about the same as in the effluent.
[c]Based on flow stress.
[d]Values estimated from the total crack extension during the test period and not from the slope of the crack length vs. time plot.

A detailed metallographic evaluation of the specimen was performed to verify the crack length measurements and to characterize the fracture morphology. Composite micrographs of the cross section and the fracture surface are shown in Figs. 53 and 54, respectively. The beach mark on the fracture surface just below the region marked #3 in Fig. 54 and extending across the width of the specimen corresponds to the end of test period 1. Fracture occurred along the plane perpendicular to the stress axis up to the beach mark, Fig. 53, and away from this plane for other test periods. Also, the fracture morphology up to the beach mark is predominantly TG, whereas some regions of IG fracture are observed in test periods with long rise times or long hold periods.
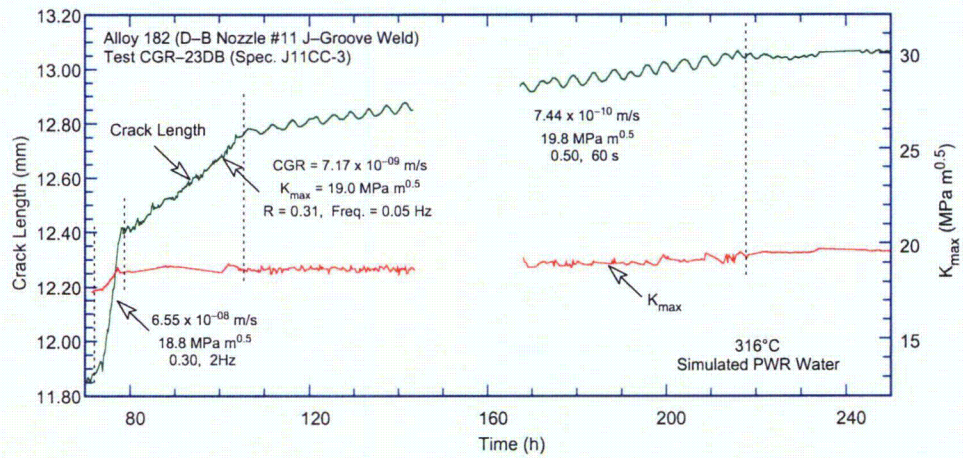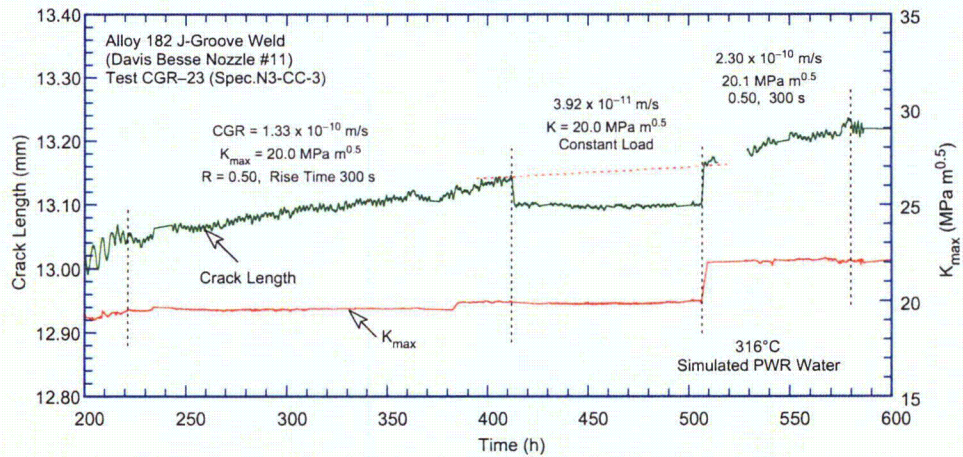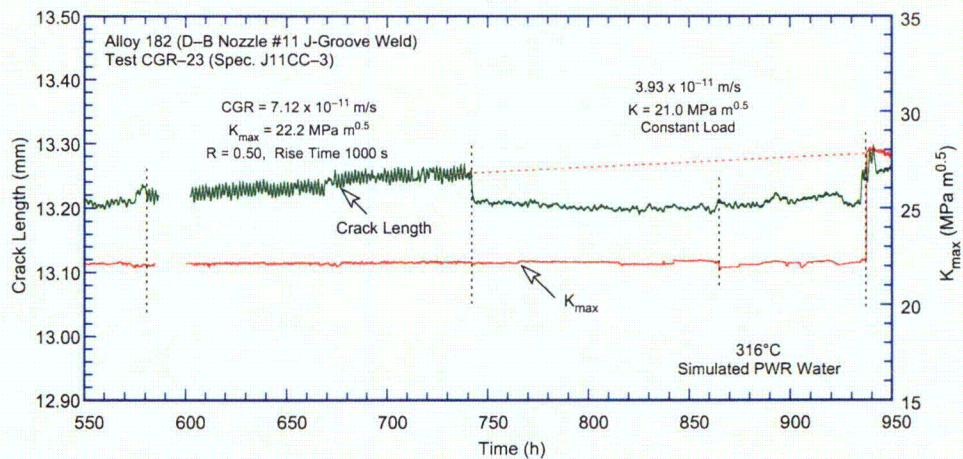
Figure 52. Crack length vs. time plots for Specimen J11CC-3 of Alloy 182 in PWR water at 316°C during (a) precracking and test period 1, (b) 2–4, (c) 5–7, and (d) 8–13.
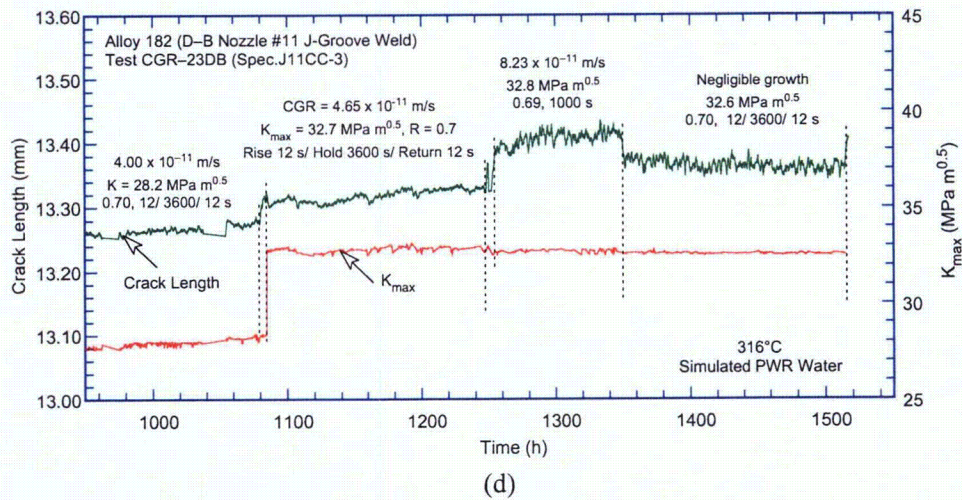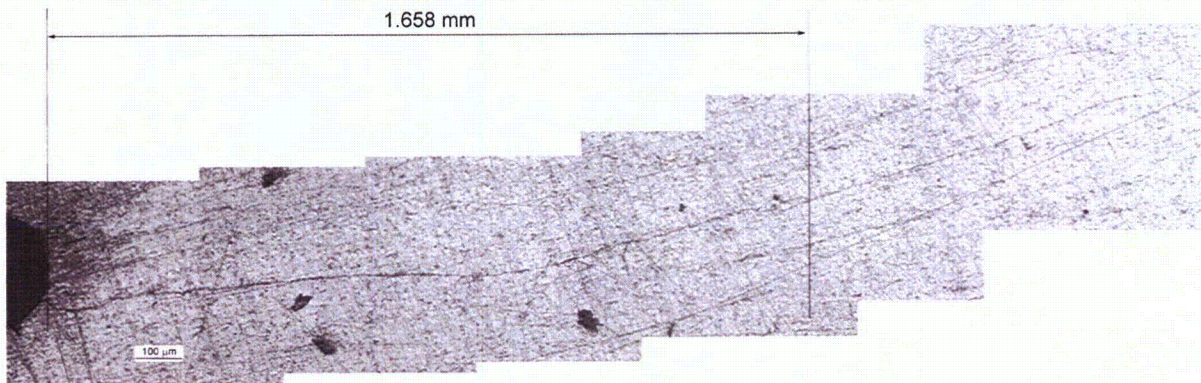
(d)

Figure 52.   (Contd.)

Figure 53.   Micrograph of the cross section of Specimen J11CC-3 showing the fracture–plane profile.
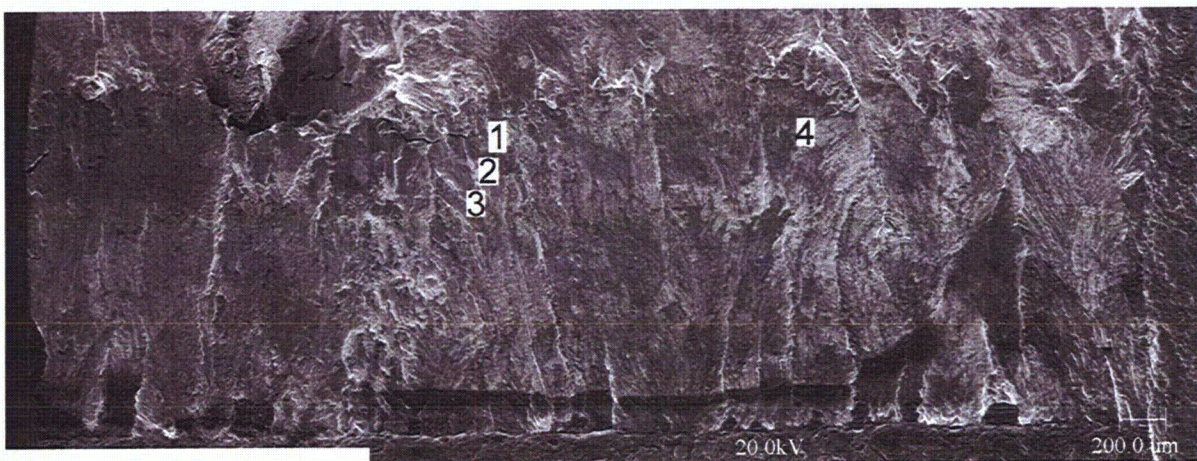

Figure 54.   Micrograph of the fracture surface of Specimen J11CC-3 tested in PWR water at 316°C.

53

The final crack length was measured from the SEM micrograph. The actual crack length was a factor of ≈2 greater than the value determined from the DC potential measurements. The experimental crack extensions were scaled proportionately. The corrected CGRs are given in Table 14.

The entire crack extension in the region marked #4 in Fig. 54 is shown in Fig. 55. The fracture mode is predominantly TG; some regions of IG fracture are observed in the final ≈200-μm crack extension (i.e., test periods 6–13). Several ridges, parallel to the direction of crack extension, are observed in the predominantly TG region of the fracture surface (i.e., test periods 1–3). As seen before in Specimen J11CC-1, the fracture surface obtained under cyclic loading with a long rise time or constant load with or without periodic unloading (test periods 5–13) shows several out-of-plane cracks suggesting crack branching at the crack tip (e.g., Fig. 56). These out-of-plane cracks may be responsible for the low growth rates observed for the material.
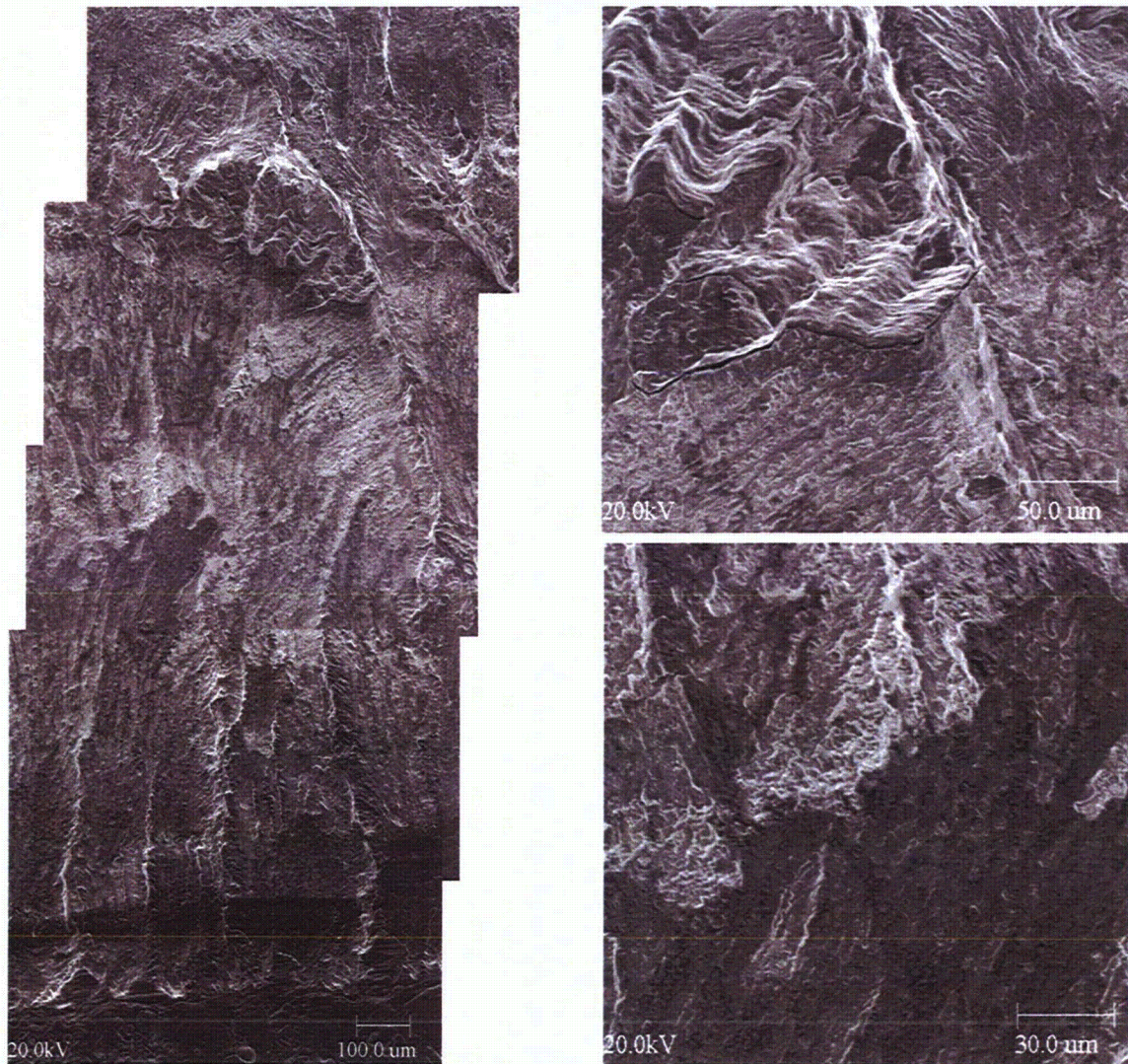

Figure 55. Micrographs showing a slice of the entire length of the fracture surface and high-magnification micrographs of the surface at select locations.
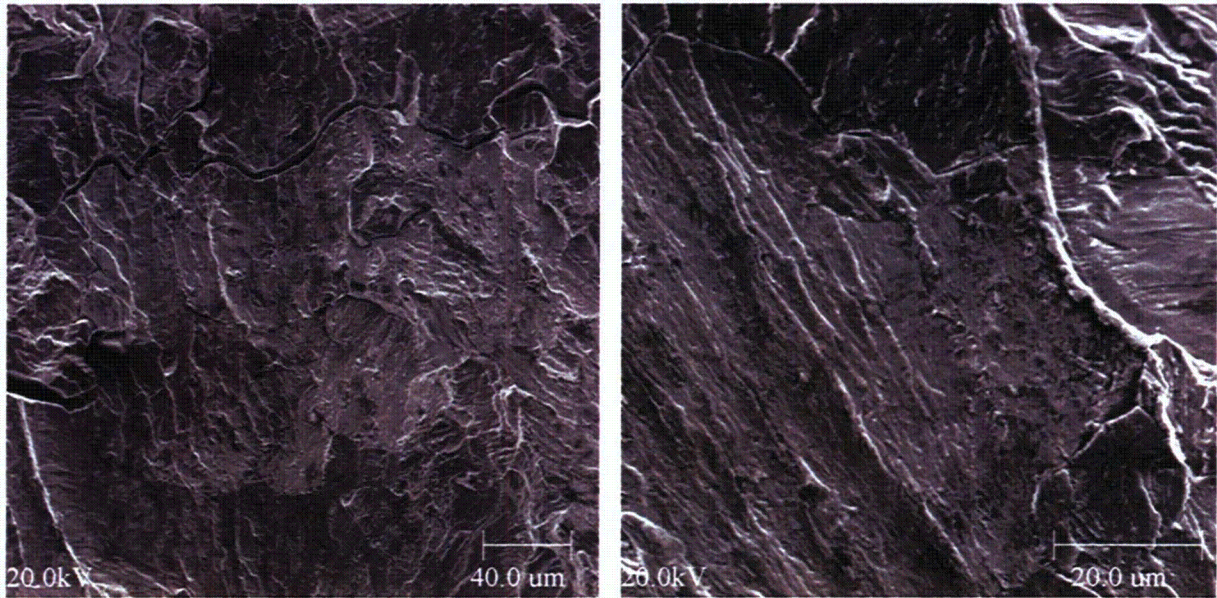
Figure 56. Micrographs showing IG secondary cracks parallel to the crack front in Specimen J11CC-3 tested in PWR water at 316°C.

4.2.3 V.C. Summer Nozzle–to–Pipe Weld

4.2.3.1 Specimen WCR-01

The first weld specimen from V.C. Summer material, made of Alloy 82, was tested in a simulated primary water environment at 320°C. Fatigue precracking was carried out at $K_{max} \approx 24.0$ MPa·m$^{1/2}$, $R \approx 0.3$, and triangular waveform with 0.5–0.1 Hz frequency. Next, R was increased incrementally to 0.5, and the loading waveform was changed to a slow/fast sawtooth with a rise time of 30 or 300 s. The crack growth data along with the test conditions, resulting stress intensity factors K_{max}, and experimental and estimated CGRs for the two specimens are given in Table 15 and Fig. 57. For this specimen, testing concluded with a constant–load period at K_{max}= 24.2 MPa·m$^{1/2}$.

Table 15. CGR data for Specimen WCR–01 of the Alloy 82 SMA weld in PWR water[a] at 320°C.

Test Period	Test Time (h)	Conduc-tivity[b] (μS/cm)	O_2 Conc.[b] (ppb)	Load Ratio R	Rise Time (s)	Down Time (s)	Hold Time (s)	Kmax[c] (MPa·m$^{1/2}$)	ΔK (MPa·m$^{1/2}$)	CGR$_{env}$ (m/s)	Estd. A182 CGR$_{air}$[d] (m/s)	Crack Length (mm)
Pre a	100	23	<10	0.32	1	1	0	24.14	16.42	2.83E-09	5.20E-08	12.289
Pre b	124	23	<10	0.31	0.5	0.5	0	24.14	16.66	4.86E-09	1.08E-07	12.351
Pre c	140	23	<10	0.29	5	5	0	23.18	16.46	1.72E-09	9.77E-09	12.379
Pre d	146	23	<10	0.30	0.25	0.25	0	23.96	16.77	9.34E-09	2.16E-07	12.484
1	258	23	<10	0.30	30	2	0	24.35	12.17	1.39E-10	7.99E-10	12.649
2	380	23	<10	0.52	30	2	0	25.17	12.08	2.06E-10	7.05E-10	12.736
3	523	23	<10	0.50	300	12	0	23.69	11.88	3.18E-11	7.52E-11	12.779
4	593	23	<10	1.00	–	–	–	24.22	0.00	4.11E-11	–	12.789

[a]Simulated PWR water with 2 ppm Li, 1100 ppm B, and 2 ppm dissolved hydrogen (≈23 cc/kg). Measured pH was 6.4.
[b]Represents values in the effluent. Feedwater conductivity was about the same as in the effluent.
[c]At the end of the test the maximum allowed K_{max} based on the final load and using Eqn. 11 was 28.8 MPa·m$^{1/2}$.
[d]Crack growth rates for Alloy 182 weld metal in air determined by Eq. 14 in Section 5.1.
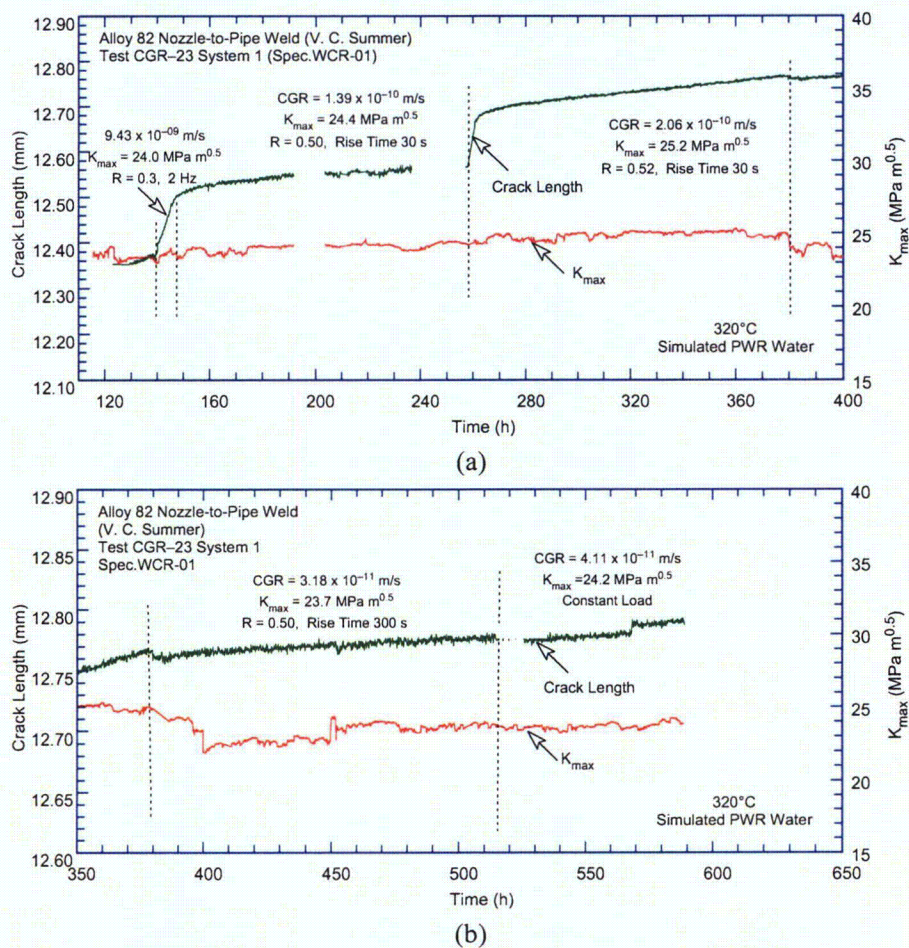
Figure 57. Crack length vs. time for Alloy 82 nozzle-to-pipe weld specimen (V.C. Summer) in simulated PWR environment at 320°C during test periods (a) Precrack–2 and (b) 3–4.

The final crack lengths were determined from metallographic examination of the fractured specimens by SEM. The entire fracture surface of WCR-01 is shown in Fig. 58. The first (green) line designates the region where IG features start to be observed, and the second (red) line shows the final crack extension. While a relatively straight crack front is observed, the appearance suggests pinning. Nevertheless, the observed features are consistent with the testing parameters. These features can be better seen in the higher magnification micrographs of Fig. 59. Figure 59a corresponds to the boxed area of Fig. 58. A mixture of TG and IG growth is observed during precracking and cyclic loading (Fig. 59a) and a predominantly IG growth during the final constant–load test (Fig. 59b).
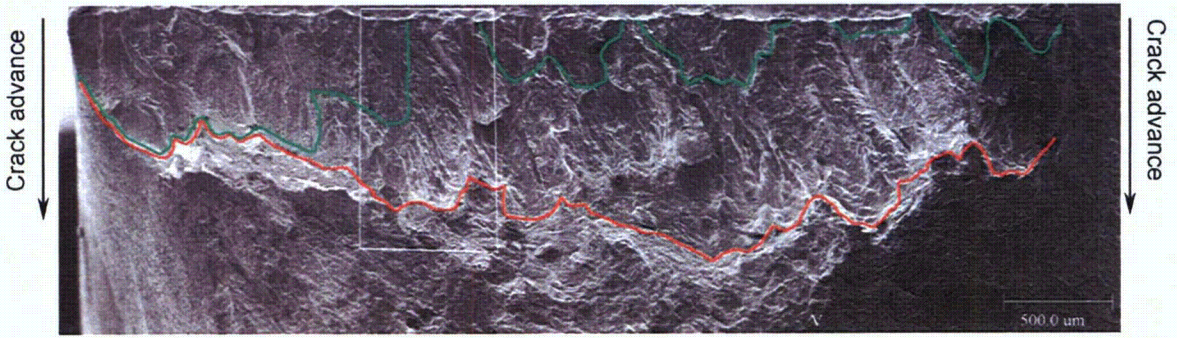
Figure 58. Micrograph of the fracture surface of Specimen WCR–01. Crack advance is from top to bottom.

(a)   (c)
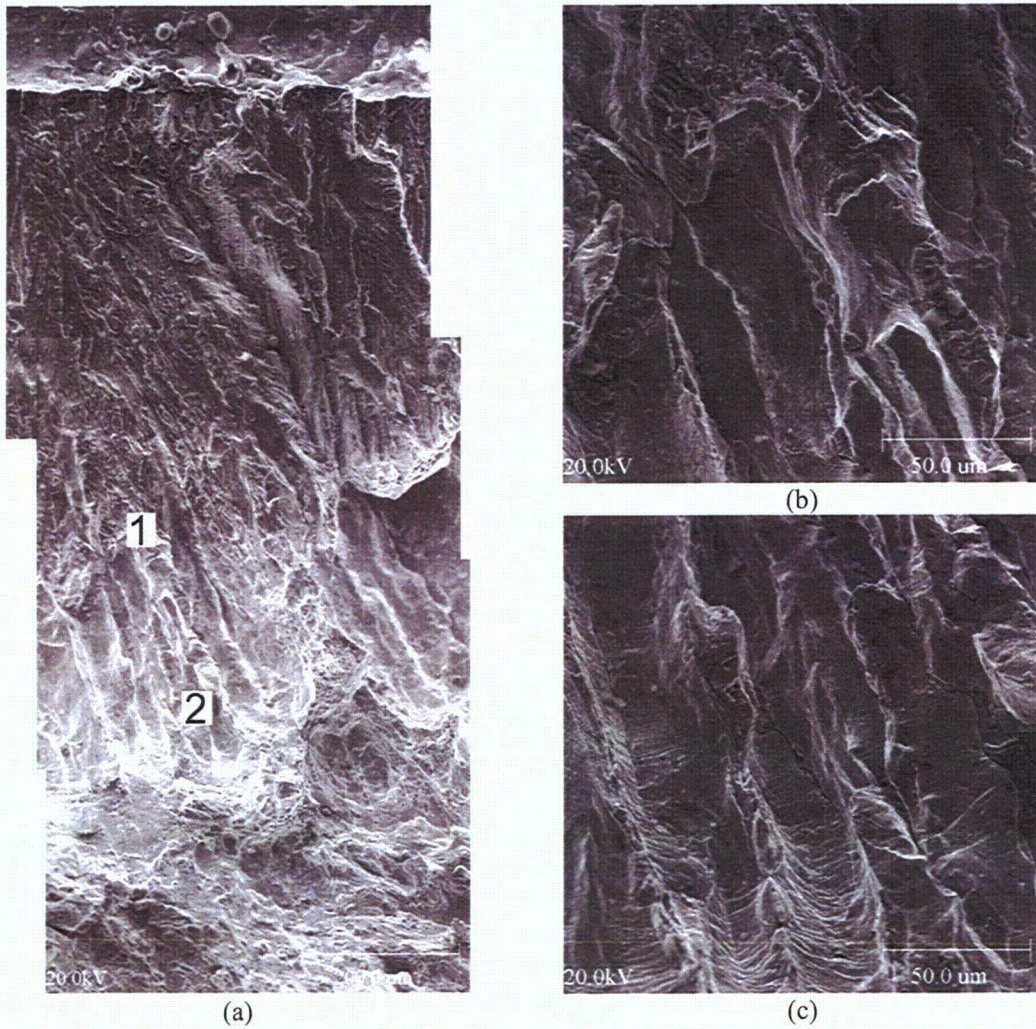
Figure 59. Micrographs of (a) portion of the fracture surface of Specimen WCR–01 (crack advance is from top to bottom), and higher magnification of (b) position 1 and (c) position 2.

On the basis of the image shown in Fig. 59, the crack extension for the entire test was measured to be 0.782 mm (0.031 in.), 2.6 times larger than the value obtained from DC potential measurements.

Especially during IG cracking, it is likely that the two separating surfaces partially touch each other, thus causing the DC potential measurements to underestimate the crack length. Since IG features appeared on the fracture surfaces starting from the early stages of testing, we corrected all crack results, including precracking, by a factor of 2.6. The data shown in Table 15 have been corrected accordingly.

4.2.3.2 Specimen BCR-01

Another test was conducted on the Alloy 182 butter specimen (BCR-01) in a simulated PWR water environment at 320°C. The specimen was fatigue precracked at $K_{max} = 21$ MPa·m$^{1/2}$, R = 0.3, and a triangular waveform. The specimen was then set at constant load at $K_{max} = 22.1$ MPa m$^{1/2}$ for approximately 300 h. Next, the specimen was cycled at R = 0.5 at increasing rise times and set again at constant load at $K_{max} = 27.0$ MPa·m$^{1/2}$. Subsequently, the specimen was cycled at R = 0.5 at increasing rise times, and set at constant load of $K_{max} = 32.1$ MPa·m$^{1/2}$. Following that, the specimen was cycled with the goal of reaching approximately $K_{max} = 36$ MPa·m$^{1/2}$, and set at constant load for the final test period. The experimental conditions and results are shown in Table 16, and the changes in crack length and K_{max} with time are shown in Fig. 60. The ECPs of a Pt electrode and a companion Alloy 600 electrode downstream from the autoclave were –620 and –650 mV (SHE), respectively. For this specimen, the test protocol consisted of four constant–load periods at K_{max} values up to 36 MPa·m$^{1/2}$.

Table 16. CGR data for Specimen BCR–01 of the Alloy 182 SMA weld in PWR water[a] at 320°C.

Test Period	Test Time (h)	Conduc-tivity[b] (μS/cm)	O$_2$ Conc.[b] (ppb)	Load Ratio R	Rise Time (s)	Down Time, (s)	Hold Time (s)	K_{max}[c] (MPa·m$^{1/2}$)	ΔK (MPa·m$^{1/2}$)	CGR$_{env}$ (m/s)	Estd. A182 CGR$_{air}$[d] (m/s)	Crack Length (mm)
Pre a	31.0	26	<10	0.30	0.25	0.25	0	21.07	14.75	4.00E-09	1.28E-07	12.046
Pre b	54.0	26	<10	0.30	0.25	0.25	0	21.91	15.34	1.82E-08	1.50E-07	12.269
Pre c	71.0	26	<10	0.31	0.25	0.25	0	22.42	15.47	2.50E-08	1.59E-07	12.407
Pre d	75.0	26	<10	0.31	0.25	0.25	0	21.91	15.12	2.42E-08	7.24E-08	12.573
1	386.0	26	<10	1.00	–	–	–	22.06	0.00	2.35E-11	–!	12.616
2a	389.0	26	<10	0.50	0.25	0.25	0	25.63	12.82	1.49E-08	1.23E-07	12.715
2b	413.0	26	<10	0.50	0.25	0.25	0	25.81	12.91	1.25E-08	1.27E-07	12.905
3	507.0	26	<10	0.50	50	2	0	26.73	13.36	3.16E-10	7.31E-10	13.041
4	839.0	26	<10	1.00	–	–	–	26.97	0.00	2.34E-11	–	13.057
5	842.0	26	<10	0.30	1	1	0	29.67	20.77	5.04E-08	1.30E-07	13.291
6a	845.0	26	<10	0.50	1	1	0	29.60	14.80	8.18E-09	5.55E-08	13.369
6b	869.0	26	<10	0.50	1	1	0	30.44	15.22	9.17E-09	6.23E-08	13.514
7	939.0	26	<10	0.50	300	12	0	30.60	15.30	2.79E-10	2.12E-10	13.569
8	1,340.0	26	<10	1.00	–	–	–	32.14	0.00	4.49E-11	–	13.594
9	1,343.0	26	<10	0.30	1	1	0	35.05	24.53	5.73E-08	2.57E-07	13.791
10	1344.0	26	<10	0.50	1	1	0	35.70	17.85	1.44E-08	1.20E-07	13.869
11	1346.0	26	<10	0.50	300	12	0	35.21	17.61	5.78E-10	3.77E-10	13.901
12	1702.0	26	<10	1.00	–	–	–	36.03	0.00	4.14E-11	–	13.930

[a]Simulated PWR water with 2 ppm Li, 1100 ppm B, and 2 ppm dissolved hydrogen (≈23 cc/kg). Measured pH was 6.4.
[b]Represents values in the effluent. Feedwater conductivity was about the same as in the effluent.
[c]At the end of the test, the maximum allowed K_{max} was 26.8 MPa·m$^{1/2}$.
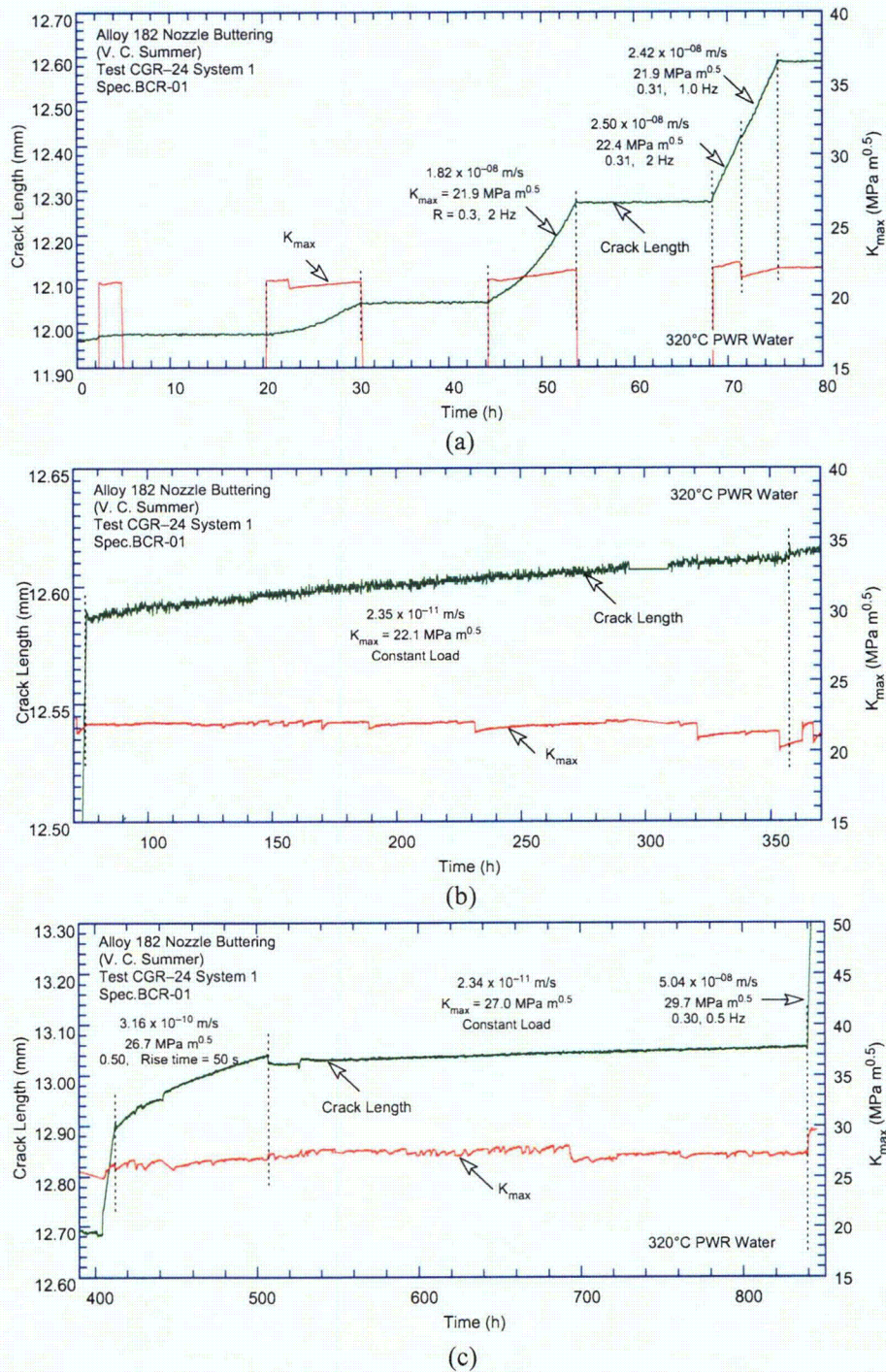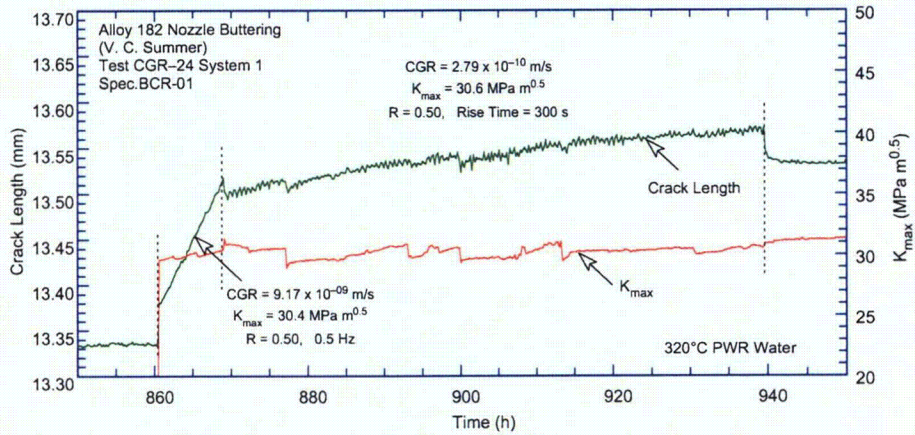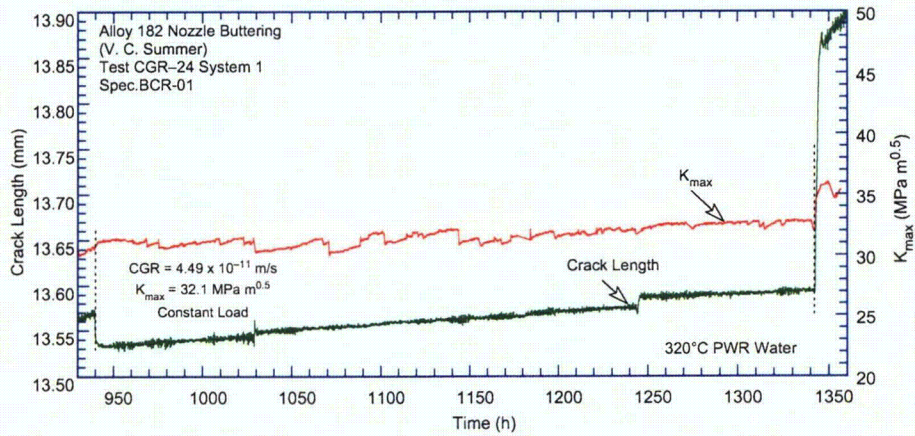[d]Crack growth rates for Alloy 182 weld metal in air determined by Eq. 14 in Section 5.1.

Figure 60. Crack length vs. time for Alloy 182 butter specimen in simulated PWR environment at 320°C during (a) precracking and test periods (b) 1, (c) 2–4, (d) 5–7, (e) 8–10, and (f) 11–12.

(d)

(e)
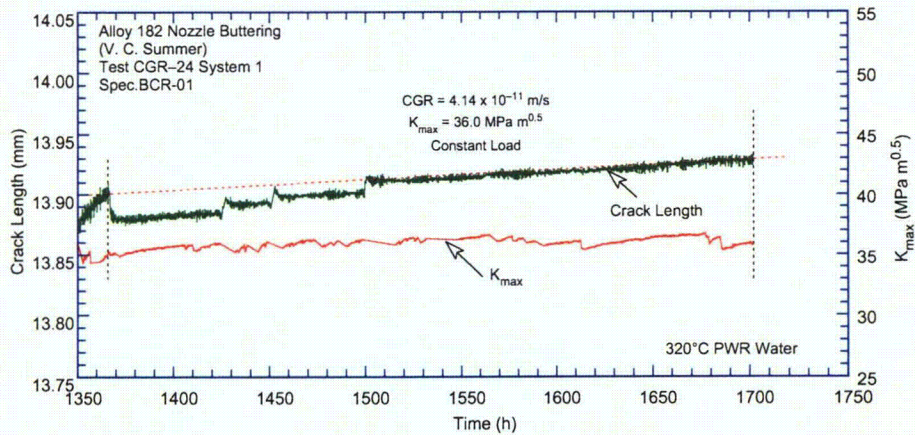
(f)

Figure 60. (Contd.)

At the conclusion of the test, the specimen was removed from the autoclave and prepared for fractographic examination. Figure 61 shows an image of the cross section of the BCR-01 specimen. The full extent of the crack was measured to be 1.848 mm (0.073 in.). The fracture surface was also examined by SEM to obtain an accurate measurement of the crack extent. Figure 62 shows the fracture surface of

Specimen BCR-01. Perhaps because of the different approach for the testing protocol with constant-load periods being separated by mechanical fatigue periods to physically mark the IG regions associated with each constant–load period, the difference between the measured crack length and that determined from the DC potential measurements was relatively small. The average crack extension was 1.980 mm (0.078 in.) compared with 1.472 mm (0.058 in.) determined from the DC potential drop method; i.e., a correction of 34%. The results shown in Table 16 and Fig. 60 have been corrected accordingly.
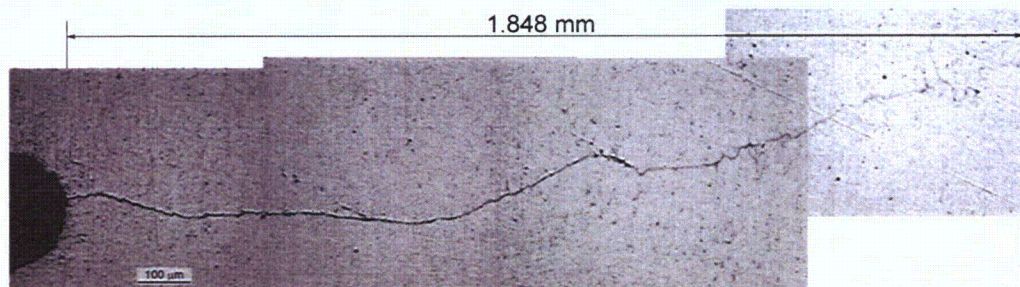
Figure 61. Cross section of the V.C. Summer Alloy 182 butter Specimen BCR-01.
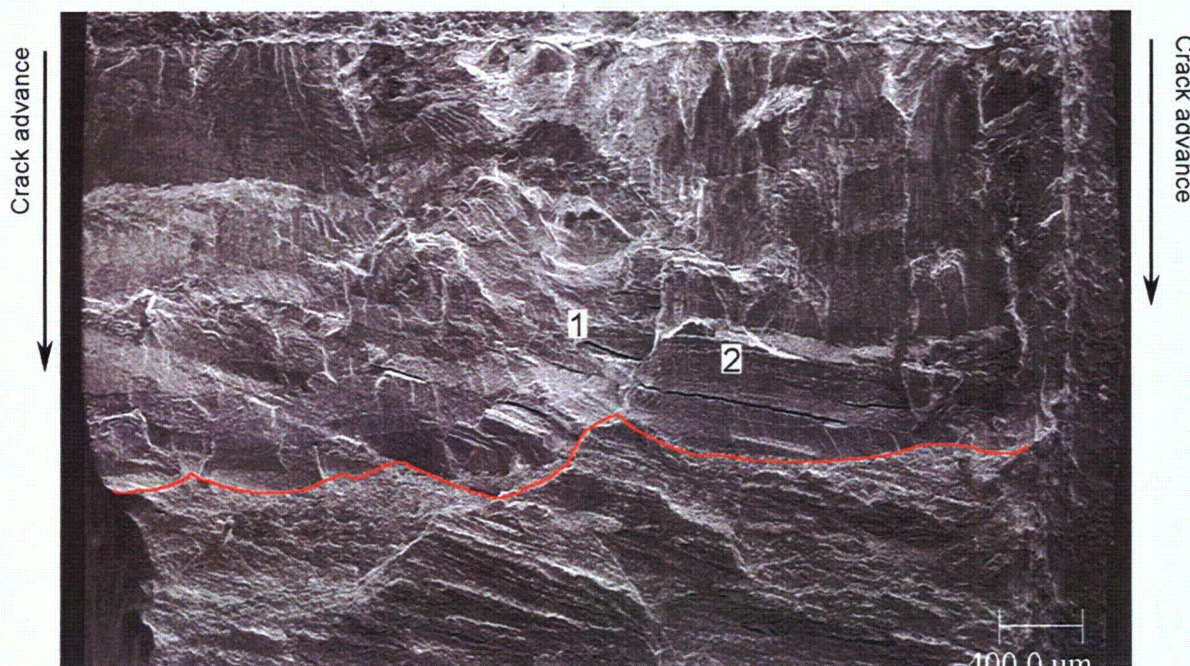
Figure 62. Micrograph of the fracture surface of Specimen BCR-01. Crack advance is from top to bottom.

As observed earlier for Specimen WCR-01, a fairly straight crack front was obtained for Specimen BCR-01 (red line in Fig. 62). Figure 63 presents two additional, high-magnification micrographs of the fracture surface taken at locations 1 (Fig. 63a) and 2 (Fig. 63b) in Fig. 62. In both micrographs, the IG fracture mode appears to be interrupted by crack branching, e.g., several secondary cracks, transverse to the crack plane, are observed along the crack front.

61

(a)   (b)

Figure 63.   Micrographs of the fracture surface of Specimen BCR–01 at locations 1 (a) and 2 (b) in Fig. 62.

4.2.3.3 Specimen WLR-01

For this weld specimen, WLR-01, fatigue precracking was carried out at $R \approx 0.3$, $K_{max} \approx 21.0$ MPa·m$^{1/2}$, and triangular waveform with 0.5–2 Hz frequency. R was then i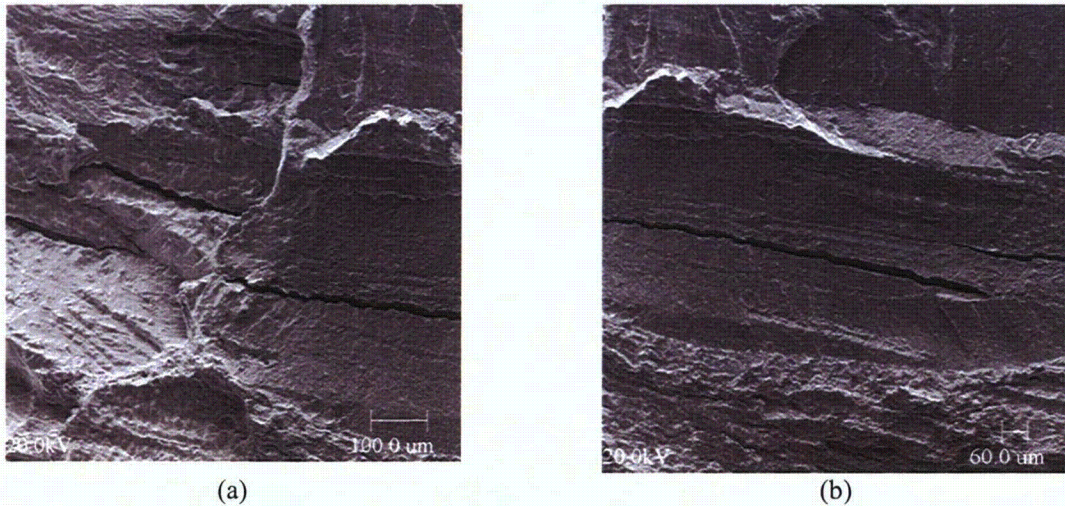ncreased incrementally to 0.7, and the loading waveform changed to a slow/fast sawtooth with rise time of 50–1000 s. The crack growth data along with the test conditions, resulting stress intensity factors K_{max}, and experimental and estimated CGRs for the two specimens are given in Table 17, and the changes in crack length and K_{max} with time are plotted in Fig. 64.

Table 17. CGR data for Specimen WLR–01 of the Alloy 82 SMA weld in PWR water[a] at 320°C.

Test Period	Test Time, (h)	Cond,[b] (μS/cm)	O$_2$ Conc.,[b] (ppb)	Load Ratio R	Rise Time, (s)	Down Time, (s)	Hold Time, (s)	K_{max},[c] (MPa·m$^{1/2}$)	ΔK, (MPa·m$^{1/2}$)	CGR$_{env}$, (m/s)	Estd. A182 CGR$_{air}$,[d] (m/s)	Crack Length, (mm)
Pre a	103	26	<10	0.30	0.5	0.5	0	20.92	14.64	8.22E-09	6.37E-08	12.640
Pre b	167	26	<10	0.30	50	2	0	20.77	10.38	2.61E-10	2.67E-10	12.719
Pre c	196	26	<10	0.30	1	1	0	17.72	8.86	1.35E-10	7.00E-09	12.729
Pre d	215	26	<10	0.30	0.5	0.5	0	20.84	10.42	2.82E-09	2.72E-08	12.837
Pre e	226	26	<10	0.30	0.25	0.25	0	20.43	14.30	1.20E-08	1.16E-07	13.017
Pre f	265	26	<10	0.50	1	1	0	24.44	12.22	1.52E-08	2.61E-08	14.251
1	315	26	<10	0.50	50	2	0	23.99	12.00	5.93E-10	4.78E-10	14.349
2	389	26	<10	0.69	1000	12	0	24.24	7.51	1.94E-10	6.86E-12	14.418
3	504	26	<10	0.67	1000	12	0	24.96	8.24	7.19E-11	8.92E-12	14.531
4	841	26	<10	1.00	–	–	–	24.67	–	2.07E-11	–	14.531
5	1082	26	<10	1.00	–	–	–	33.19	–	5.43E-12	–	14.590
6	1203	26	<10	0.70	1000	12	0	32.85	9.85	2.04E-11	2.20E-11	14.590
7	1392	26	<10	0.70	300	12	0	33.26	9.98	1.94E-11	7.71E-11	14.602
8	1398	26	<10	0.30	0.5	0.5	0	36.77	25.74	1.03E-07	6.40E-07	15.614
9	1417	26	<10	0.50	100	12	0	40.37	20.19	7.01E-09	2.05E-09	16.099
10	1439	26	<10	0.50	300	12	0	44.24	22.12	5.84E-09	1.00E-09	16.410
11	1466	26	<10	0.50	50	2	0	46.13	23.07	2.03E-09	6.95E-09	16.656
12	1531	26	<10	0.50	300	12	0	47.09	23.55	8.95E-10	1.25E-09	16.854
13	1634	26	<10	0.50	1000	12	0	49.15	24.57	4.12E-10	4.48E-10	16.964
14	2469	26	<10	1.00	-	-	-	52.50	–	7.71E-11	–	17.182

[a]Simulated PWR water with 2 ppm Li, 1100 ppm B, and 2 ppm dissolved hydrogen ($\approx$23 cc/kg).
[b]Represents values in the effluent.
[c]At the end of the test, the maximum allowed K_{max} was 22.6 MPa·m$^{1/2}$.
[d]Crack growth rates for Alloy 182 weld metal in air determined by Eq. 14 in Section 5.1.
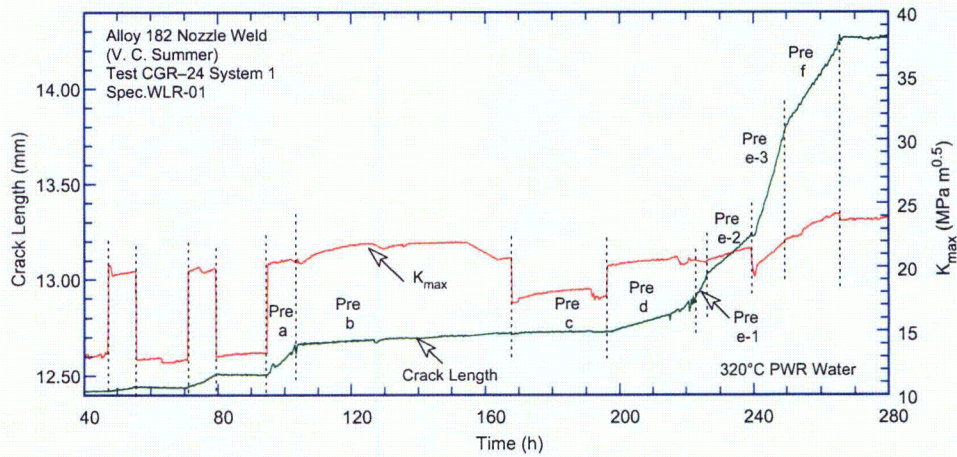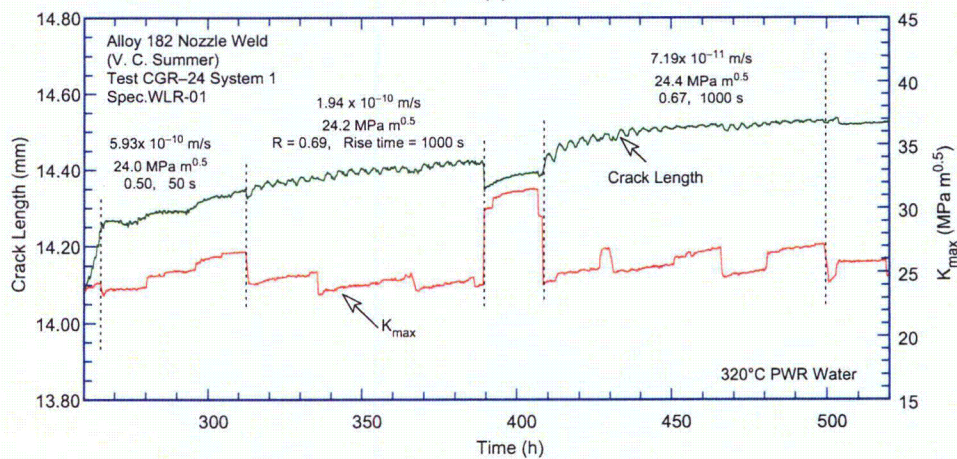
Figure 64.   Crack length vs. time for Alloy 82 weld Specimen WLR-01 in simulated PWR environment at 320°C during (a) precracking, (b) precracking and 1–3, (c) 4, (d) 5, (e) 6–7, (f) 8-9, (g) 11–13, and (h) 14.

63

(d)

(e)

(f)

Figure 64.   (Contd.)

64
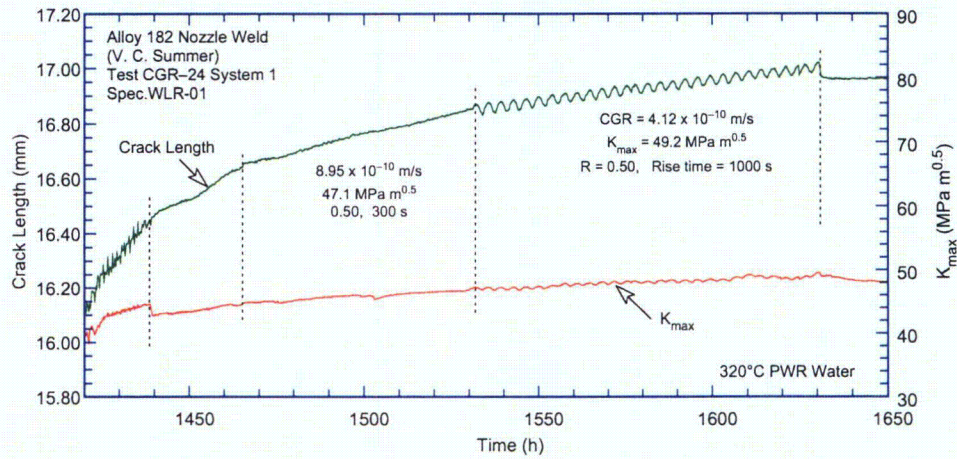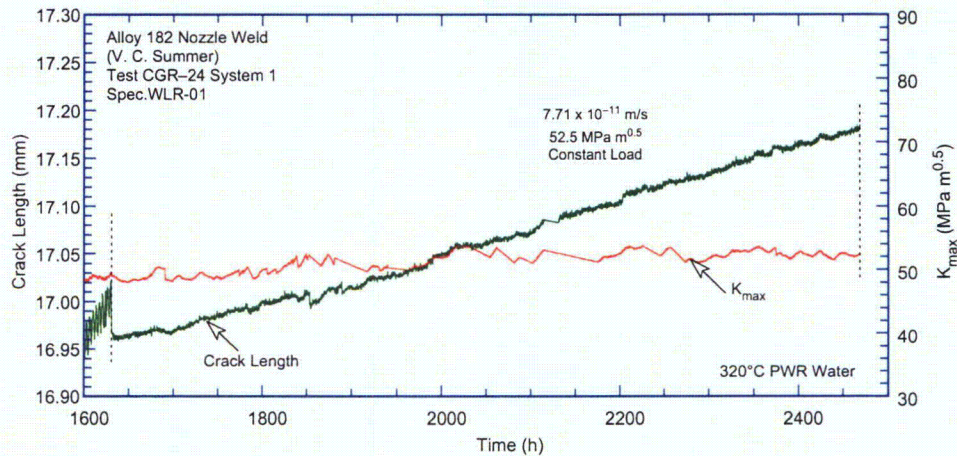
Figure 64.　　(Contd.)

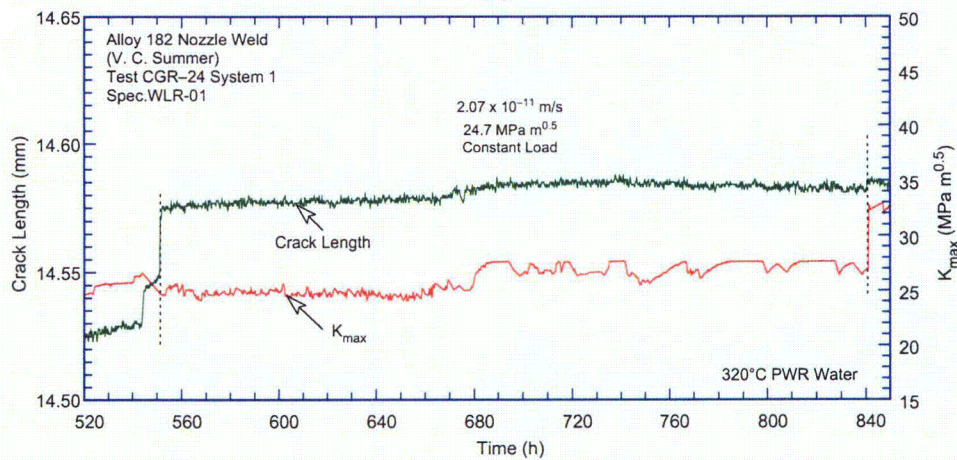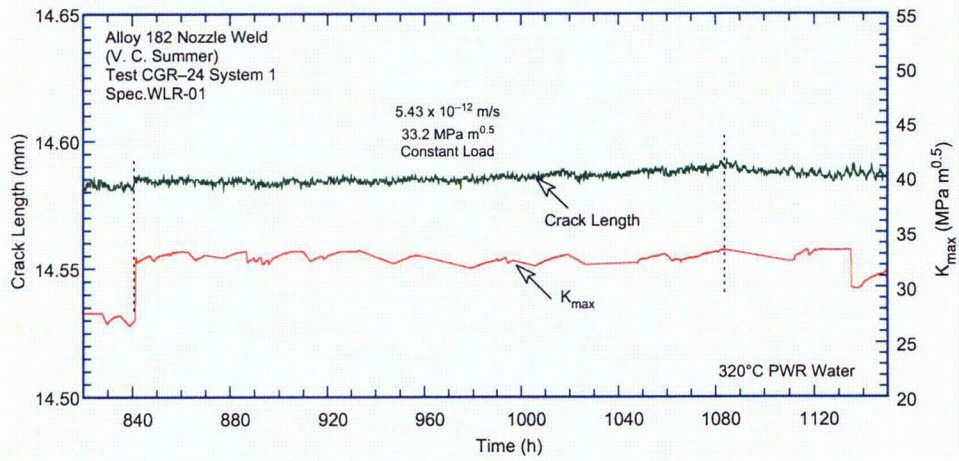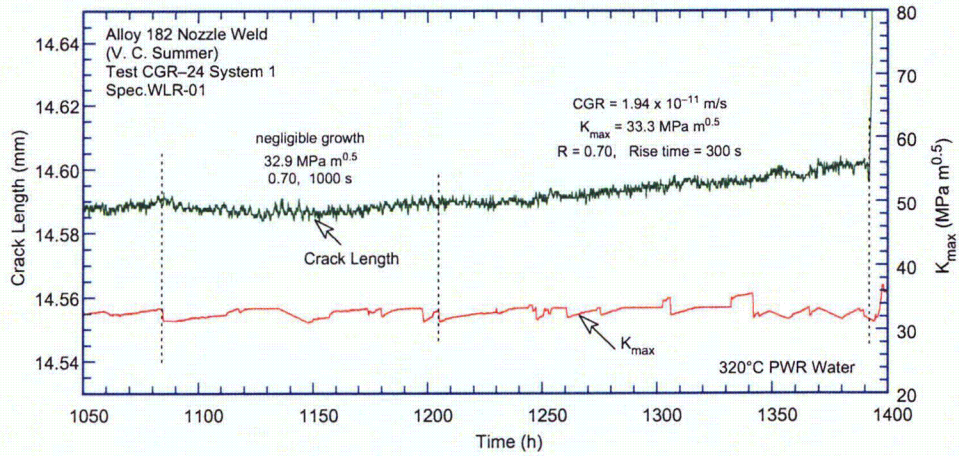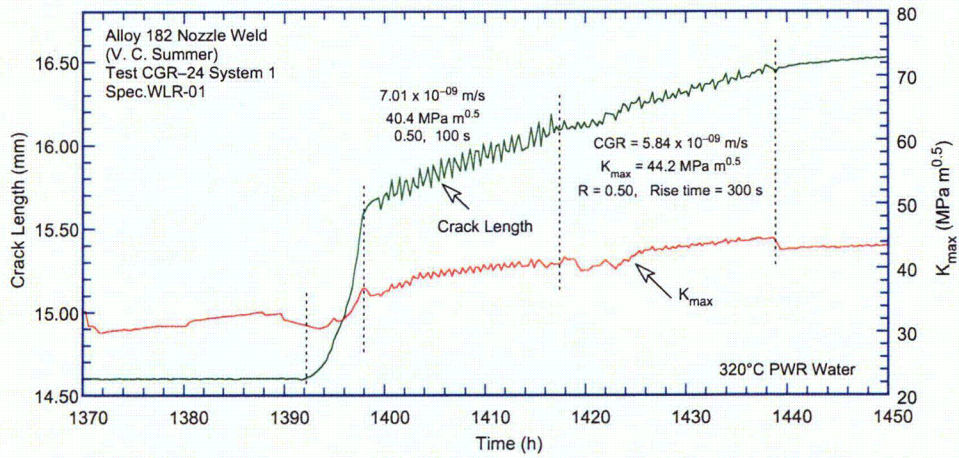The fracture surface of WLR–01 is shown in Figs. 65 and 66. Cracking initiated in a TG mode under cyclic loading, changed to IG during the long rise-time periods of the test, and remained IG during the constant–load periods. Initiating the crack under cyclic loading and then transitioning to constant load with long rise-time cyclic loading seems to have resulted in a relatively straight crack front. The green and red lines mark the IG region. Secondary IG cracks were observed in the IG region, consistent with the previous observations on other V.C. Summer specimens. The IG region (green and red lines) was designated so as to encompass all these secondary cracks, based on the assumption that they initiated and grew during the constant–load period.

A comparison between DC potential data and measurements based on the SEM micrograph yielded correction factors of 1.69 for the TG region and 1.91 for the IG region. The relatively large correction factor for the TG region is consistent with the observation of some IG features within the TG region. The experimental conditions and corrected crack lengths are given in Table 17, and the changes in crack length and K_{max} with time based on the corrected results are shown in Fig. 64.

Figure 65. Micrograph of the fracture surface of the weld V.C. Summer Specimen WLR–01. Crack advance is from top to bottom.

(a)

(b)

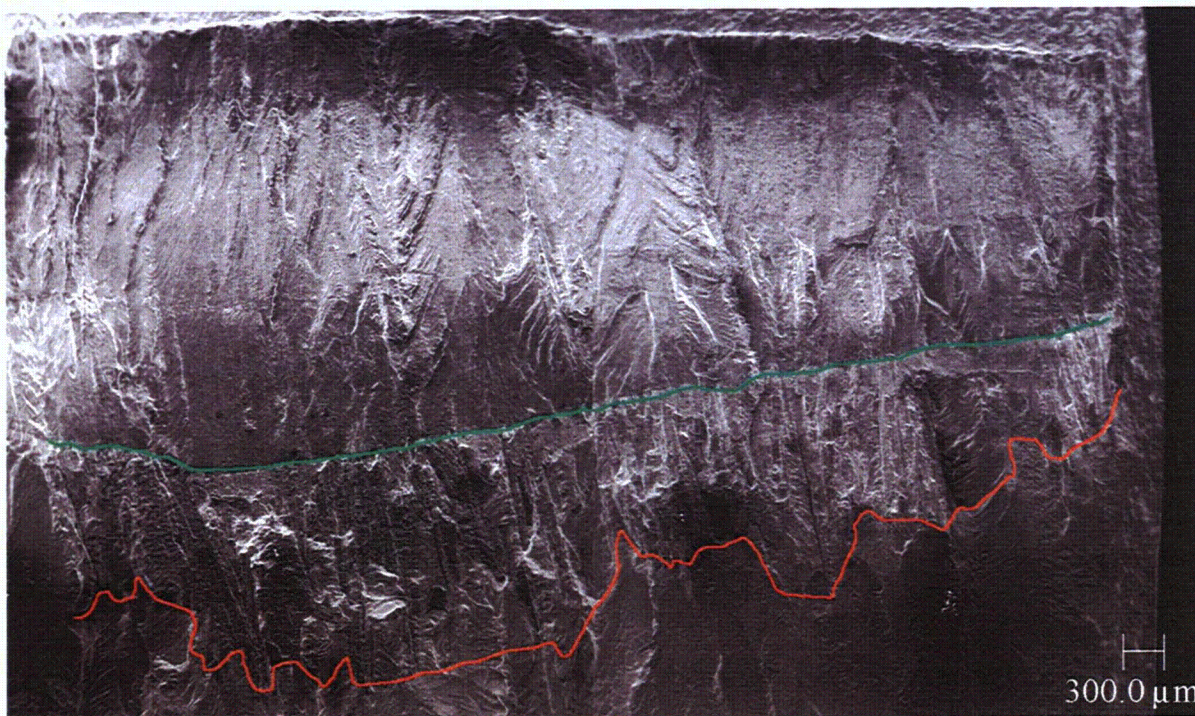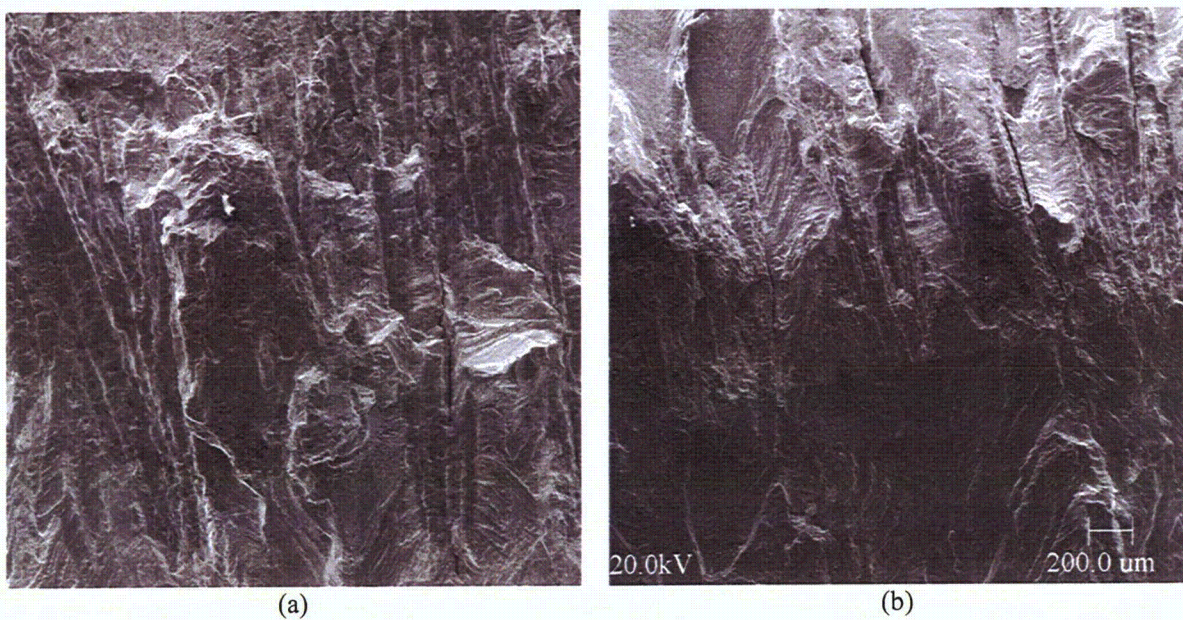Figure 66 Micrographs of the fracture surface of Specimen BCR–01 at locations (a) 1 and (b) 2 in Fig. 65.

5 Discussion

This section discusses the cyclic and constant-load CGRs for the Davis-Besse CRDM nozzle Alloy 600 and J–groove weld Alloy 182, and for the V.C. Summer Alloy 182 butter and Alloy 82 weld alloys. It also addresses issues relating to the comparison of field and laboratory-prepared welds.

5.1 Alloy 600 from Davis-Besse CRDM Nozzle #3

The experimental CGRs under cyclic loading are compared in Fig. 67 with those predicted in air under the same loading conditions. Such plots allow direct comparison of cyclic CGR data obtained at different test temperatures, load ratios, and frequencies. Although the results show considerable scatter, environmental enhancement of growth rates is observed in all specimens of the Davis–Besse CRDM nozzle alloy. Also, specimen orientation does not seem to have any effect on growth rates, e.g., the CGRs for Specimens N3CL–1 and N3CC–3 are comparable, and those for Specimen N3CC–2 are slightly lower. For comparison purposes, the cyclic CGRs for Alloy 600 from the Davis–Besse CRDM Nozzle #3 in PWR water may be represented by the best–fit curve for Alloy 600 in normal water chemistry (NWC) for the BWR environment (i.e., Eq. 3 for Alloy 600 in ≈300 ppb DO at 289°C), although the environment is totally unrelated to that of interest. The experimental CGRs for Specimens N3CL–1 and N3CC–3 are slightly higher than the curve, and those for Specimen N3CC–2 are lower.
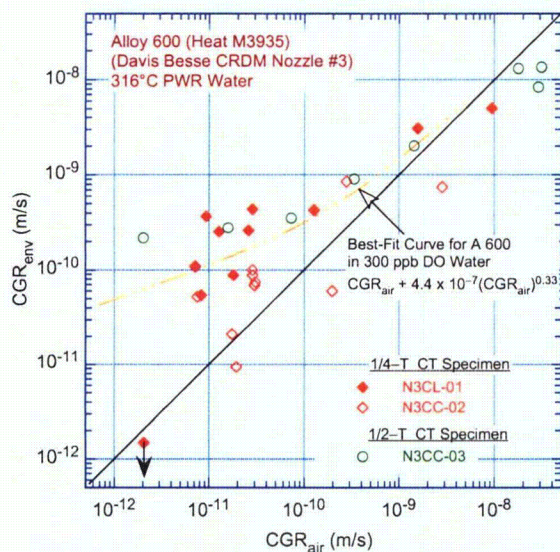
Figure 67.
CGR data for Davis–Besse CRDM Nozzle #3 Alloy 600 in PWR water at 316°C under cyclic loading.

The fatigue CGR data obtained earlier at ANL indicated that in low–DO water, environmental enhancement of CGRs in Alloy 600 seems to depend on material conditions such as yield strength and grain boundary coverage of carbides.[30] Materials with high yield stress and/or poor grain–boundary carbide coverage showed environmental enhancement. The results of the Davis–Besse CRDM Nozzle #3 Alloy 600 appear to be inconsistent with this trend, e.g., the nozzle #3 alloy has relatively low yield stress (Table 8) and appears to have good grain–boundary carbide coverage (Fig. 19). However, the loading conditions for the present tests are different from those for the earlier tests. In Alloy 600, environmental enhancement of CGRs is typically observed when load ratio R is ≥0.5, and rise time for the loading cycle is ≥30 s. For the earlier tests,[30] although the load ratios were in the range of 0.6–0.9, the rise time for all tests was only 12 s.

The fracture mode does not seem to influence the cyclic CGRs of the Davis–Besse CRDM Nozzle #3 Alloy 600. Although the fracture surface of N3CC–3 (Fig. 45) shows a larger fraction of TG fracture than that of N3CL–1 (Fig. 39), the CGRs for the two specimens are comparable.

The experimental CGRs under constant load, with or without partial unloading, are plotted as a function of applied K_{max} in Fig. 68a. The median and 75th percentile CGR curves based on the best fit of the data for 26 heats of Alloy 600 (Eq. 4) are also included in the figure. The CGR curves at 316°C were calculated using an activation energy of 130 kJ/mol. The growth rates for the Davis–Besse nozzle Alloy 600 are a factor of 4–8 higher than the median curve.
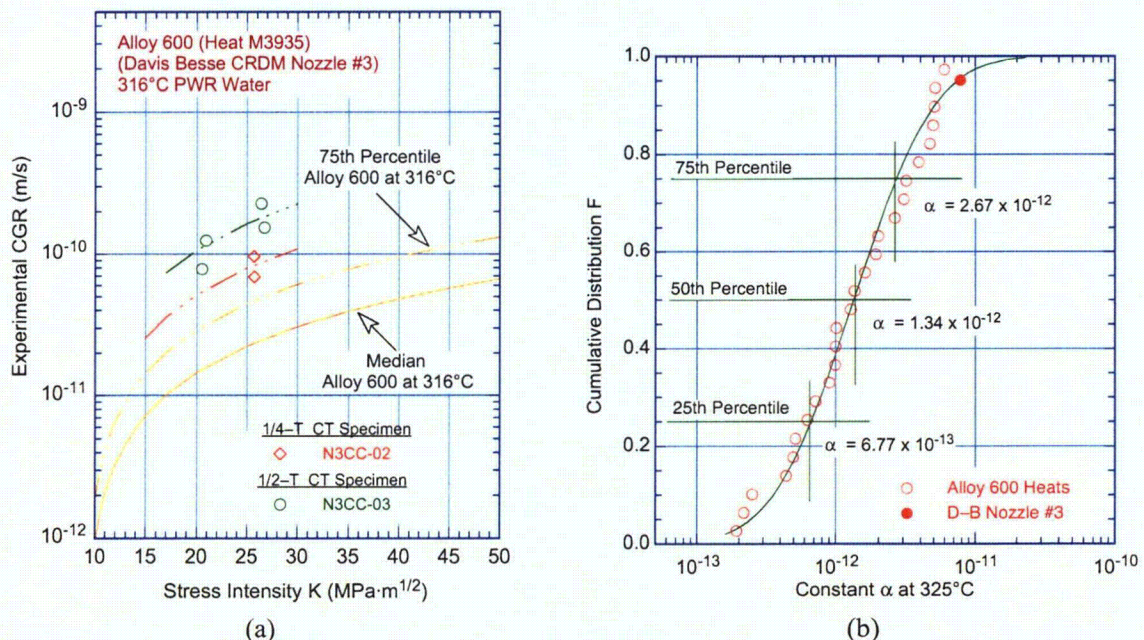
Figure 68. (a) CGR data for Davis–Besse CRDM Nozzle #3 Alloy 600 in PWR water at 316°C under constant load and (b) log–normal distribution of constant α for 26 heats of Alloy 600 [36].

The cumulative distribution of the log–normal fit to the ordered median ranking of the constant α for various data sets of Alloy 600 is shown in Fig. 68b. The experimental CGRs for Alloy 600 from Davis–Besse CRDM Nozzle #3 correspond to the ≈95 percentile of the distribution; i.e., the nozzle material exhibits very high susceptibility to SCC compared to other heats of Alloy 600.

5.2. Fatigue CGRs for Ni–alloy Weld Metals in Air

The database on fatigue CGR (da/dN) on Ni–alloy weld metals (e.g., Alloys 182, 82, 152, and 52) in air is very limited.[43–47] The database has results from ≈35 tests on Alloy 182 and 4 on Alloy 52; nearly 75% of the data are at room temperature and the remaining are at 320°C. An additional 94 tests on Alloys 82, 182, 52, and 152 weld metals in PWR water at low load ratios (e.g., ≤0.3) and/or high frequency (e.g., ≥0.1 Hz) may be included in the analysis because, under these loading conditions, CGRs are controlled primarily by mechanical fatigue. However, even these combined data on Ni–alloy weld metals are inadequate to establish the effects of stress ratio R, cyclic frequency, and stress intensity factor range ΔK on the CGRs. Consequently, the functional forms for effects of frequency, R, and ΔK in Eq. 1 were assumed to be the same as those for Alloy 600. The temperature dependence of constant C was

determined from data sets that were normalized for the effects of R and ΔK (Fig. 69). The CGR (m/cycle) of Ni–alloy welds, such as Alloys 82, 182, 52, and 152, in air may be expressed as

$$da/dN = C_{Niweld} (1 - 0.82\ R)^{-2.2} (\Delta K)^{4.1}, \tag{14}$$

where ΔK is in MPa·m$^{1/2}$, and C_{Niweld} is given by a fourth-order polynomial of temperature T(°C), expressed as

$$C_{Niweld} = 8.659 \times 10^{-14} - (5.272 \times 10^{-17})T + (2.129 \times 10^{-18})T^2$$
$$- (1.965 \times 10^{-20})T^3 + (6.038 \times 10^{-23})T^4. \tag{15}$$

The predicted–vs.–experimental CGRs for Ni–alloy weld metals at various temperatures in air and PWR environment under predominantly mechanical fatigue loading conditions are shown in Fig. 70. The predicted values show good agreement with the experimental results. Under similar loading conditions, the fatigue CGRs of Ni–alloy welds in air are a factor of 2–3 higher than those of Alloy 600.
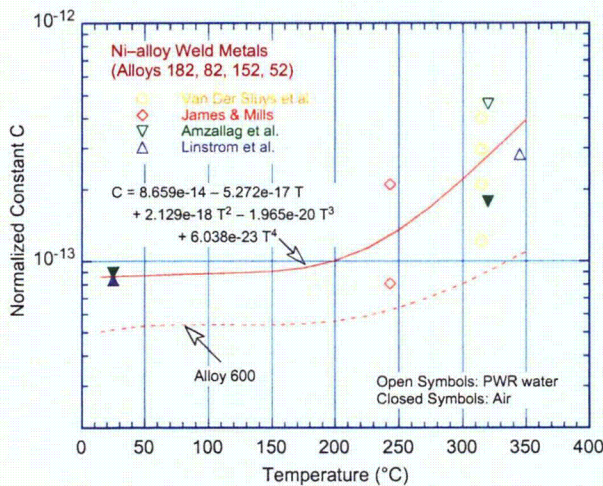

Figure 69.
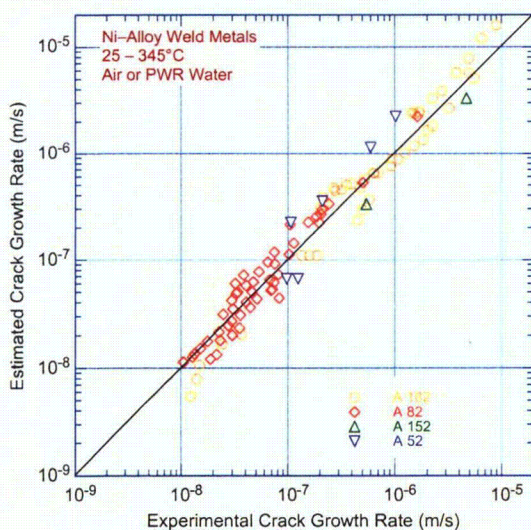Variation of normalized constant C for Ni–alloy weld metals with temperature.

Figure 70.
Predicted–vs.–experimental values of fatigue CGR of Ni–alloy weld metals in air and PWR environment under predominantly mechanical fatigue loading conditions.

Figure 71 shows the experimental-vs.–predicted values of fatigue CGR of Alloys 182 (Fig. 71a) and 82 (Fig. 71b) in air and in a PWR environment.[43-47] Although not all of the data were used for determining Eq. 15, both data sets are in good agreement with the predicted values. Limited data are available for Alloys 182 and 82 for high R and low frequencies. They indicate that the enhancement due to the PWR environment is modest. The data for Alloy 182 for $CGR_{air} < 10^{-9}$ m/s where environmental enhancement might be expected to be increasing is very limited. However, the Alloy 82 data suggest that effects may be relatively small and that the cyclic CGRs of Ni–alloy welds in PWR water may either be bounded by $5 \times CGR_{air}$ or may be represented by the expression

$$CGR_{env} = CGR_{air} + 0.018\,(CGR_{air})^{0.78}. \tag{16}$$

(a)   (b)
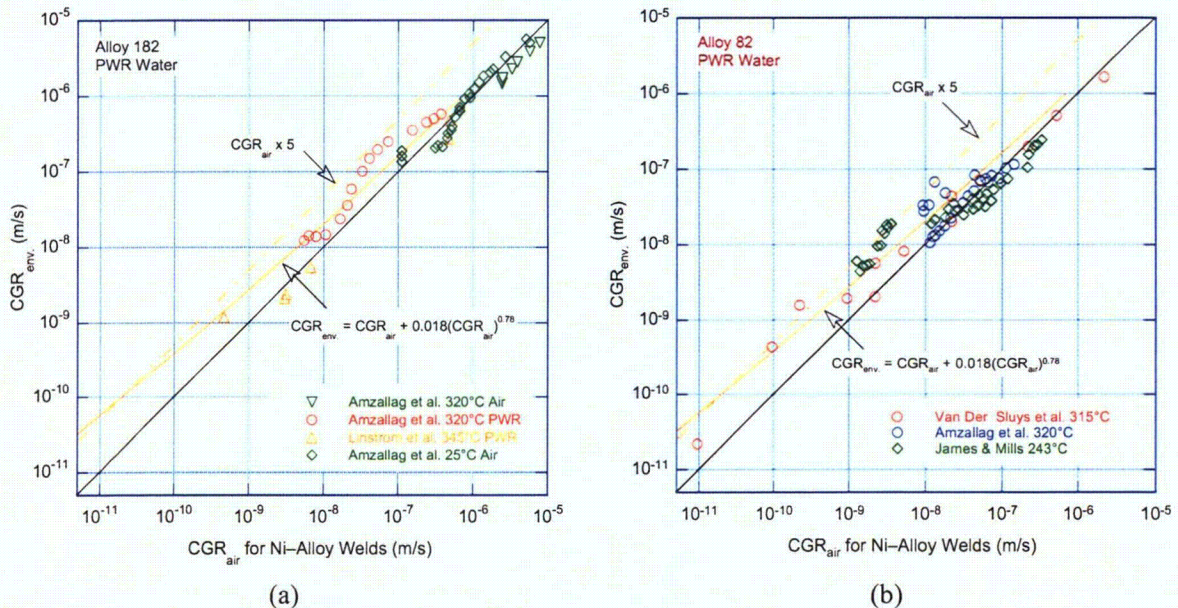
Figure 71. Experimental-vs.–predicted values of fatigue CGR of (a) Alloy 182 and (b) Alloy 82 in air and in a PWR environment [Refs. 42–46].

5.3 Ni–Alloy Welds

5.3.1 From Davis–Besse CRDM Nozzle #11

The experimental CGRs for Alloy 182 weld specimens from the Nozzle #11 J–groove under cyclic loading and those predicted for Ni-alloy welds in air under the same loading conditions are shown in Fig. 72a. The cyclic CGRs for the 1/2–T CT specimen show some environmental enhancement whereas those for the 1/4–T CT specimen show little or no enhancement. The cyclic CGRs for Alloy 182 from the D–B CRDM Nozzle #11 J–groove weld may be represented by Eq. 16. The CGRs obtained under constant load (with or without periodic partial unloading) are shown in Fig. 72b. Under constant load, the CGRs for the 1/2–T CT specimen are slightly higher than those for the 1/4–T CT specimen. However, in a PWR environment, the growth rates for the Davis–Besse J–groove weld alloy are an order of magnitude lower than the proposed disposition curve for Alloy 182 welds.[37] Figure 74b shows that the measured CGRs correspond to about the 20th percentile for the population of Alloy 182 welds.

The root cause for the low SCC growth rates is not clear. However, several out–of–plane cracks are observed along the crack front (Fig. 50). These cracks may be preexisting (e.g., hot cracks) or may

70

have formed during the tests (e.g., crack branching at the crack tip). These out–of–plane cracks appear to impede crack advance and may be responsible for the low CGRs in the material.

(a)   (b)

Figure 72.   Cyclic CGR data for Alloy 182 from the Davis–Besse CRDM Nozzle #11 J–groove weld in a PWR environment at 316°C under (a) cyclic loading and (b) constant load.

5.3.2   From V.C. Summer Reactor Vessel Nozzle–to–Pipe Weld
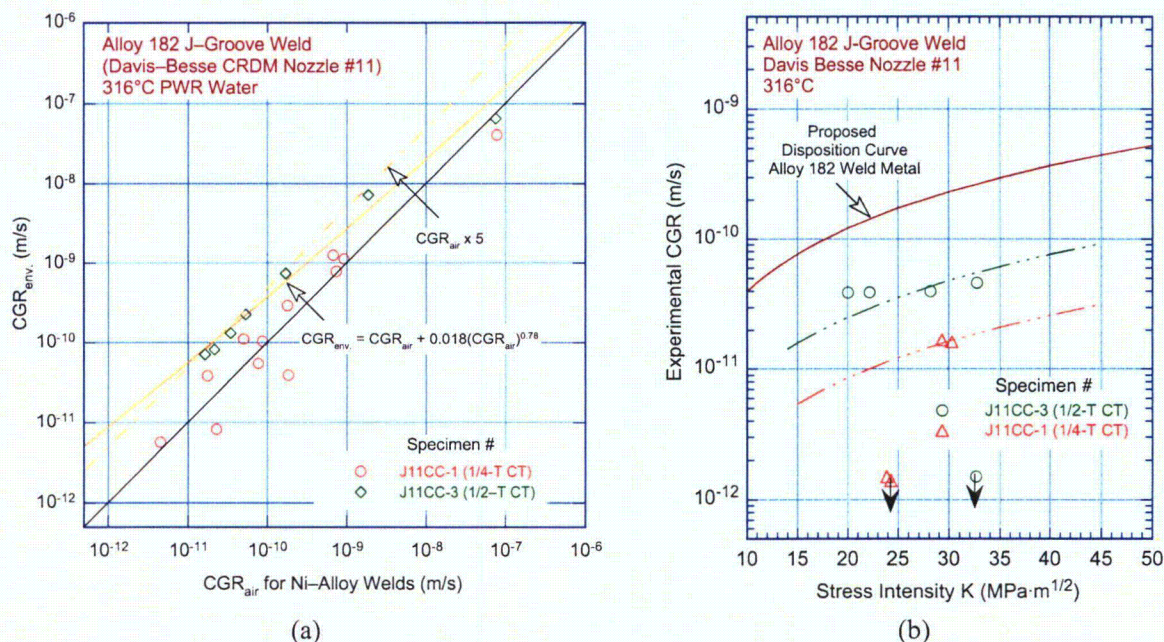
Figure 73 shows the CGR rates under cyclic loading for the three V.C. Summer Ni-alloy weld specimens, WCR–01, BCR–01, and WLR–01, as a function of the CGRs predicted for Ni-weld alloy in air under the same loading conditions. When environmental enhancement occurs, the relative CGRs in the PWR environment compared with those in air should be increasing with decreasing CGRs in air. The results indicate that under predominantly mechanical fatigue loading conditions (i.e., low load ratios and high frequency), the CGRs for the V.C. Summer weld alloys are a factor of ≈5 lower than those typically observed for laboratory–prepared Alloy 182 or 82 welds. The growth rates for the weld alloys are even lower than the rates typically observed in Alloy 600. Some environmental enhancement of CGRs is observed under loading conditions that result in CGRs less than 1×10^{-9} m/s in air (i.e., load ratios ≥0.5 and rise times ≥30 s), particularly for Specimen WLR–01 (shown as open diamonds in Fig. 73). These conditions also result in a change in fracture morphology (e.g., from TG to predominantly IG fracture).

The results also indicate that the alloy type (Alloy 82 weld or Alloy 182 butter material) or the weld structure (specimen orientation) has little or no effect on the fatigue CGRs of these materials. For example, the CGRs of the Alloy 82 weld material (Specimens WLR–01 and WCR–01) are comparable to those of the Alloy 182 butter material (Specimen BCR–01). Also, in Specimens WLR-01 and WCR-01, although the crack growth direction is along the dendrites whereas in Specimen BCR–01 it is across the dendrites, the CGRs under similar environmental and loading conditions are comparable for all specimens. These results are consistent with the existing fatigue CGR data for Ni–alloy welds in a PWR environment.[43–47]

71
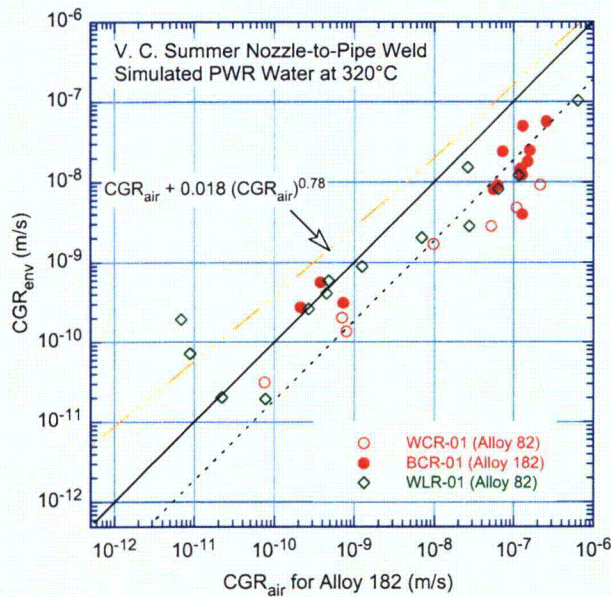
Figure 73.
Fatigue CGR data for V.C. Summer Ni–alloy welds in a PWR environment plotted as a function of the growth rate for Ni-alloy welds in air under the same loading conditions.

Figure 74a shows CGR data under constant load for the V.C. Summer weld alloys. Results from Jacko et al.[53], on the same alloys, are also included in the figure. The CGR for Specimen WLR-01 at $K_{max} = 31.2$ MPa·m$^{1/2}$ (period 5, Table 17) was considered anomalous, and thus not included in Fig. 74a. The CGRs of Alloy 82 weld material (Specimens WLR–01 and WCR–01) with growth direction along the dendrites are comparable to those of the Alloy 182 butter material (Specimen BCR–01) with growth

(a)

(b)
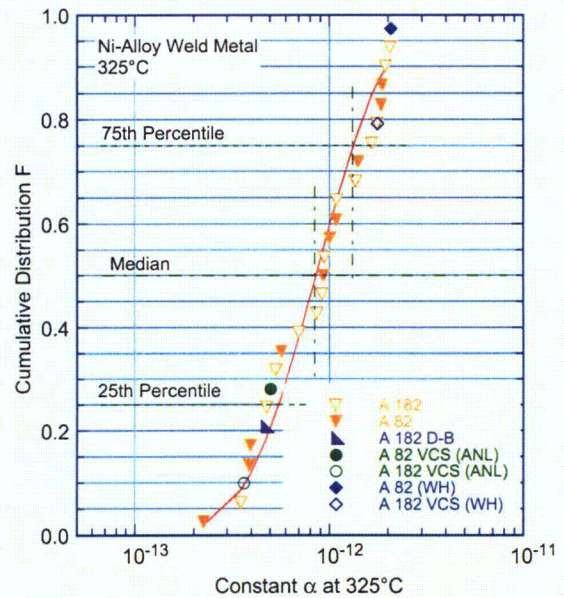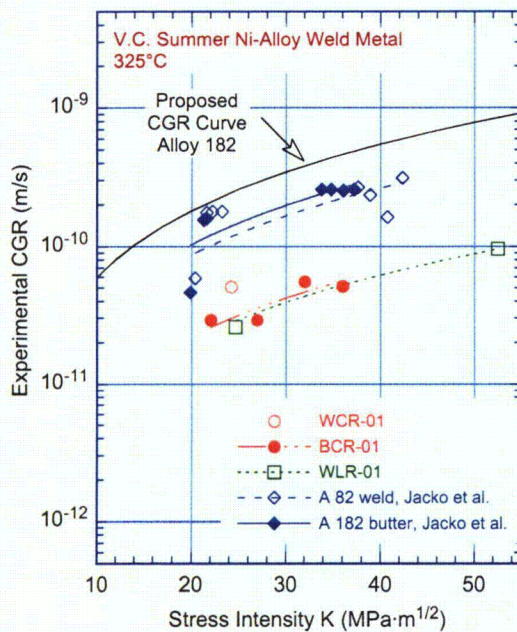
Figure 74. (a) CGR data for Alloy 182 and 82 nozzle-to-pipe butter and weld specimens from V.C. Summer in PWR environment at 325°C under constant load and (b) log–normal distribution of constant α for several heats of Alloys 82 and 182.

direction transverse to the dendrites. In general, CGRs in Alloy 182 are a factor of 2.5 higher than in Alloy 82; however, the rates along a direction transverse to the dendrites are a factor of ≈2 lower than those parallel to the dendrites. The effects of alloy type and specimen orientation seem to have cancelled each other, yielding approximately the same growth rates for the weld and butter alloys. However, the CGRs from the present study are a factor of ≈4 lower than those obtained by Jacko et al.[53] Also, the CGRs for the V.C. Summer alloys from the present study are comparable to those determined for the Davis–Besse CRDM nozzle J–groove weld.

Figure 74b shows the cumulative distribution of the log–normal fit to the ordered median ranking of the constant α in Eq. 5 for various data sets of Ni-base weld alloys available in the literature. It essentially is a ranking of the various heats with respect to their susceptibility to SCC. The results of Jacko et al.[53] suggest that the V.C. Summer weld and butter alloys correspond to the ≈95 and 80 percentile, respectively, of the distribution of the various heats, whereas, the results from the present study indicate that they correspond to the ≈25 and 10 percentile, respectively. The reasons for the differences in the results between the two studies is not clear. The crack fronts in the tests reported here are relatively straight. The crack fronts in the tests in Jacko et al.[53] do not appear to be as straight. CGRs in isolated "fingers" may be more rapid than the overall growth of a straight crack front.

5.4 Variability in Ni-Alloy CGR Data

The Alloy 600 material from Davis-Besse Nozzle #3 (Heat M3935) is highly susceptible to SCC and ranks at the estimated 95th percentile of heats of Alloy 600 that have been investigated to develop the CGR disposition curve for this alloy in PWR environments. The proposed disposition curve is based on the 75th percentile of the CGR distribution for the available heats; the data for the Davis–Besse CRDM Nozzle #3 alloy is above the disposition curve. The reasons for the high growth rates for this alloy are still unclear.

On the basis of the observed microstructure and tensile strength of the Davis–Besse CRDM nozzle Alloy 600, the experimental CGRs are somewhat of a surprise. Materials with a good GBC of carbides (Fig. 19) and relatively low or average tensile yield stress (Table 8) are generally considered to have low susceptibility to SCC in PWR water.[48–57] The high susceptibility of the material to SCC cannot is inconsistent with expectations based on the tensile strength and microstructure of the alloy.

The most striking result for the Davis–Besse nozzle Alloy 600 is that the cracking mode was IG from the start in two of the three samples tested. The finding that IG growth takes place in a regime dominated by mechanical fatigue (which would be expected to result in a TG growth) suggests that the grain boundaries have undergone some form of sensitization during fabrication and/or the two decades of service. The fact that not all three specimens exhibited IG fracture from the beginning suggests that some regions in the nozzle may be more susceptible than others.

The composition of the Davis–Besse nozzle alloy is within ASTM specifications. It is also for the most part within the range of compositions of the heats that have been used to develop the CGR disposition curve for thick–section Alloy 600 in PWR environments.[36] The only exception is the rather low Fe content in the Davis–Besse nozzle alloy, e.g., 5.93 wt.% in the nozzle alloy compared with the range of 7.0–9.5 wt.% for the heats used to develop the disposition curve. The significance of the low Fe content on SCC susceptibility of the alloy is not clear.

Metallographic examination of the alloy did not indicate any unusual features that would explain the relatively high growth rates in this alloy. Although Ti–rich precipitates were observed in the material,

they do not seem to affect the fracture behavior (Fig. 43c). The precipitation of Ti carbides can reduce the concentration of free carbon in the matrix to a level at which it may limit the formation of the desirable grain–boundary chromium carbides. However, the Davis–Besse nozzle Alloy 600 shows good GBC of carbides. It also has a significant amount of intragranular carbides. An earlier detailed microstructural characterization of Ni–alloys by conventional metallographic and analytical electron microscopy techniques[58] indicated that materials that appear to be similar by optical metallographic analysis can exhibit pronounced microstructural differences in terms of the extent and nature of carbide precipitation. The materials most resistant to SCC were found to contain continuous or semicontinuous intergranular Cr–rich M_7C_3 carbides with a dendritic morphology and little or no distribution of intragranular carbides. A more detailed microstructural characterization of the Davis–Besse CRDM nozzle alloy may provide helpful information in understanding the susceptibility of these alloys to PWSCC.

The Alloy 182 or 82 materials from the Davis–Besse CRDM nozzle J–groove weld or the V.C. Summer reactor vessel nozzle–to–pipe weld and butter appear to be quite resistant to cracking compared to the available data. The proposed disposition curves for Ni–alloy welds, which are based on the 75th percentile of the CGR distribution for the available heats, are conservative for the weld alloys from the V.C. Summer and Davis–Besse reactors. This is true even for the CGRs determined by Jacko et al.[53]

(a)   (b)
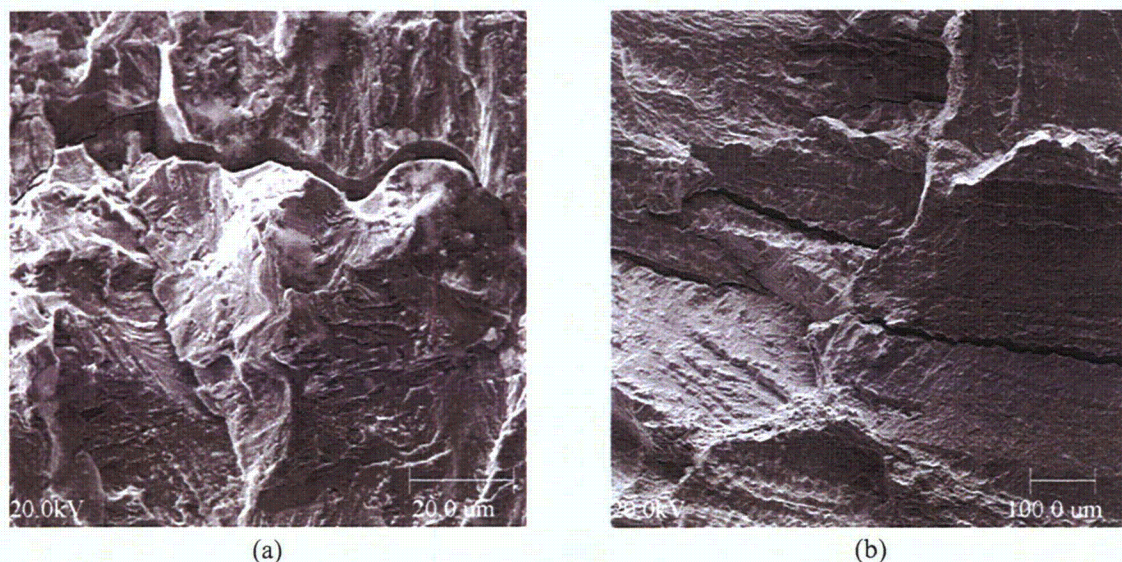
Figure 75. Micrographs from the fracture surface of weld specimens: (a) Davis-Besse Specimen J11CC–1 and (b) V.C. Summer Specimen BCR–01.

The appearance of the fracture surfaces of the weld alloys suggests that pinning by defects and precipitates could play a role by impeding crack propagation. In addition to the "pinned" fracture surfaces, another common feature observed in all specimens, with the exception of one of the V.C. Summer specimens, is the cracks on the fracture surface parallel to the crack front and transverse to the crack plane, where the propagating SCC cracks seem to arrest. Micrographs are shown from Davis-Besse Specimen J11CC-1 (Fig. 75a) and V.C. Summer Specimen BCR–01 (Fig. 75b). The only specimen that did not exhibit such cracks was WCR-01 (see, for example, Fig. 58), and this specimen had the highest measured CGR of all weld specimens. At present, it is not clear whether these are preexisting cracks (e.g., hot cracks) or whether they were formed during the tests (e.g., by crack branching at the crack tip). In any case, these out–of–plane cracks appear to impede crack advance and may be responsible for the low CGRs in the material.

74

6 Summary

Crack growth rates have been determined in tests conducted in a PWR environment at 316°C on Alloy 600 removed from the Davis–Besse CRDM Nozzle #3, and Alloy 182 from Nozzle #11 J–groove weld, as well as at 320°C on Alloys 82 and 182 from the "A" hot–leg nozzle–to–pipe weld from the V.C. Summer reactor coolant system. The purpose of these tests was to determine whether the crack growth in these materials from the Davis–Besse and V.C. Summer plants are consistent with our understanding of CGRs in Ni–alloy and welds. The results are compared with the existing CGR data to determine the relative susceptibility of these alloys to PWSCC. The tensile properties, microstructure, and fracture morphology of the nozzle material have also been characterized. The significant results are summarized as follows:

(a) For the Davis–Besse CRDM nozzle Alloy 600, the microstructure along the longitudinal plane is similar to that along the circumferential plane; the grain size varies from 30–200 μm with an average value of ≈75 μm. The material appears to have good GBC of Cr–rich carbides and a few carbides randomly distributed in the matrix. The tensile strength of the material is comparable to the typical (average) value observed for thick-section Alloy 600 products.

(b) The SCC CGRs of the Alloy 600 nozzle are a factor of 4–8 higher than those of the median curve for Alloy 600. The growth rates correspond to the ≈95th percentile of the various data sets used in developing the median curve, i.e., the nozzle material exhibits very high susceptibility to SCC. The material exhibits predominantly IG fracture, even during predominantly mechanical fatigue. A TG fracture is observed at the very beginning of the test (i.e., near the machine notch), but, in most cases, it changes to IG fracture when the first grain boundary is encountered.

(c) The reasons for the high growth rates for the nozzle Alloy 600 are not clear. Materials with good GBC of carbides and relatively low or average tensile yield stress are generally considered to have low susceptibility to SCC in PWR water. Differences in the microstructure in terms of extent and nature of carbide precipitation (e.g., absence of Cr–rich M_7C_3 carbides with a dendritic morphology) may be important for susceptibility of Alloy 600 to PWSCC.

(d) The cyclic CGRs of the Alloy 600 nozzle in PWR water at 316°C show significant environmental enhancement of growth rates. The specimen orientation does not seem to have any effect on CGRs. Although a matter of coincidence, the cyclic CGRs in PWR water at 316°C can be represented by the curve obtained for Alloy 600 in a NWC BWR environment at 289°C.

(e) The weld alloys from both the Davis–Besse and V.C. Summer plants show a typical dendritic microstructure. Tensile yield strength is higher and ductility is lower for the Davis-Besse Alloy 182 J–groove weld compared with the Alloy 600 nozzle material. The yield and ultimate strengths of Alloy 182 specimens from the butter region of the V.C. Summer weld are higher than those of Alloy 82 specimens from the weld region. This difference in tensile strength is essentially because of differences in the orientation of the dendritic structure and not differences in alloy composition; dendrites are parallel to the stress axis in the weld specimens and transverse to the stress axis for the butter specimens.

(f) For the Davis–Besse Alloy 182 weld and the V.C. Summer Alloy 82 weld and Alloy 182 butter materials, the SCC CGRs under constant load are a factor of 5 to 10 lower than the disposition curve proposed for Alloy 182 weld metals. The growth rates correspond to the ≈10th to 25th

percentile of the various heats used in developing the disposition curve, i.e., the field weld alloys exhibit low susceptibility to SCC.

(g)   Correlations have been developed to determine the CGRs of Ni–alloy welds in air as a function of loading conditions and temperature. In air, the growth rates of weld alloys are a factor of ≈2.5 greater than those of Alloy 600 under similar loading conditions.

(h)   The cyclic CGRs for Alloy 182 and Alloy 82 weld specimens from either the Davis–Besse CRDM nozzle J–groove weld or V.C. Summer reactor vessel nozzle–to–pipe weld showed very little environmental enhancement. Under predominantly mechanical fatigue loading conditions (i.e., low load ratios and high frequency), the CGRs for the V.C. Summer weld alloys are a factor of ≈5 lower than those typically observed for laboratory–prepared Alloy 182 or 82 welds.

References

1. Scott, P., "An Analysis of Primary Water Stress Corrosion Cracking in PWR Steam Generators," Proc. of the Specialists Meeting on Operating Experience with Steam Generators, Brussels, Belgium, pp. 5–6, 1991.

2. Cattant, F., "Lessons Learnt from the Examination of Tubes Pulled from Electricite de France Steam Generators," Nucl. Eng. Des. 168, pp. 241–253, 1997.

3. Diercks, D. R., W. J. Shack, and J. Muscara, "Overview of Steam Generator Tube Degradation and Integrity Issues," Nucl. Eng. Des. 194, pp. 19–30, 1999.

4. U.S. NRC Information Notice No. 90–49, "Stress Corrosion Cracking in PWR Steam Generator Tubes," Aug. 1990.

5. U.S. NRC Information Notice No. 91–43, "Recent Incidents Involving Rapid Increases in Primary-to–Secondary Leak Rate," July 1991.

6. U.S. NRC Information Notice No. 94–05, "Potential Failure of Steam Generator Tubes with Kinetically Welded Sleeves," Jan. 1994.

7. U.S. NRC Information Notice No. 89–33, "Potential Failure of Westinghouse Steam Generator Tube Mechanical Plugs," March 1989.

8. U.S. NRC Information Notice No. 89–65, "Potential for Stress Corrosion Cracking in Steam Generator Tube Plugs Supplied by Babcock and Wilcox," Sept. 1989.

9. U.S. NRC Information Notice No. 94–87, "Unanticipated Crack in a Particular Heat of Alloy 600 Used for Westinghouse Mechanical Plugs for Steam Generator Tubes," Dec. 1994.

10. U.S. NRC Information Notice No. 90–10, "Primary Water Stress Corrosion Cracking (PWSCC) of Inconel 600," Feb. 1990.

11. U.S. NRC Generic Letter 97-01, "Degradation of Control Rod Drive Mechanism and Other Vessel Closure Head Penetrations," April 1, 1997.

12. Economou, J., A. Assice, F. Cattant, J. Salin, and M. Stindel, "NDE and Metallurgical Examination of Vessel Head Penetrations," 3rd Intl. Symp. of Fontevraud, Sept. 12–16, 1994.

13. Robinson, M. R., Duke Power Company, "Oconee Unit 1 and Unit 3 Reactor Vessel Head Leakage, Cracking of RV Head Penetrations due to Primary Water Stress Corrosion Cracking," NRC Meeting with the NEI EPRI Material Reliability Program Regarding CRDM Nozzle Cracking Issues, Rockville, MD, April 12, 2001.

14. Frye, C. R., T. Alley, M. L. Arey, Jr., and M. R. Robinson, "Cracking in Alloy 600/182 Reactor Vessel Head Penetrations," PVP–Vol. 437, Service Experience and Failure Assessment Applications ASME 2002, P. S. Lam, ed., American Society of Mechanical Engineers, New York, pp. 171–178, 2002.

15. U.S. NRC Information Notice 2001–05, "Through–Wall Circumferential Cracking of Reactor Pressure Vessel Head Control Rod Driver Mechanism Penetration Nozzle at Oconee Nuclear Station, Unit 3," April 30, 2001.

16. U.S. NRC Bulletin 2001–01, "Circumferential Cracking of Reactor Pressure Vessel Head Penetration Nozzles," Aug. 3, 2001.

17. U.S. NRC Information Notice 2000–17, "Crack in Weld Area of Reactor Coolant System Hot Leg Piping at V.C. Summer," Oct. 18, 2000; Suppl. 1, Nov. 16, 2000; Suppl. 2, Feb. 28, 2001.

18. Jenssen, A., K. Norrgard, J. Lagerstrom, G. Embring, and D. Tice, "Assessment of Cracking in Dissimilar Metal Welds," Proc. of the Tenth Intl. Conf. on Environmental Degradation of Materials in Nuclear Power Systems-Water Reactors, NACE International, Houston, TX, 2001.

19. Bennetch, J. I., G. E. Modzelewski, L. L. Spain, and G. V. Rao, "Root Cause Evaluation and Repair of Alloy 82/182 J–Groove Weld Cracking of Reactor Vessel Head Penetrations at North Anna Unit 2," PVP–Vol. 437, Service Experience and Failure Assessment Applications ASME 2002, P. S. Lam, ed., American Society of Mechanical Engineers, New York, pp. 179–185, 2002.

20. U.S. NRC Information Notice 2002–11, "Recent Experience with Degradation of Reactor Pressure Vessel Head," March 12, 2002.

21. U.S. NRC Information Notice 2003–11, "Leakage Found on Bottom–Mounted Instrumentation Nozzles," Aug. 13, 2003; Suppl. 1, Jan. 8, 2004.

22. U.S. NRC Bulletin 2003–02, "Leakage from Reactor Pressure Vessel Lower Head Penetrations and Reactor Coolant Pressure Boundary Integrity," Aug. 21, 2003.

23. Licensee Event Report 414-2001-002, Rev. 0, Nov. 12, 2001, U.S. Nuclear Regulatory Commission.

24. Licensee Event Report 255-1993-009, Rev. 1, Nov. 18, 1993, U.S. Nuclear Regulatory Commission.

25. Ruther, W. E., W. K. Soppet, and T. F. Kassner, "Corrosion Fatigue of Alloys 600 and 690 in Simulated LWR Environments," NUREG/CR–6383, ANL–95/37, April 1996.

26. Ruther, W. E., W. K. Soppet, and T. F. Kassner, "Environmentally Assisted Cracking of Alloys 600 and 690 in Simulated LWR Water," Environmentally Assisted Cracking in Light Water Reactors, Semiannual Report, July 1997–December 1997, NUREG/CR–4667, Vol. 25, ANL–98/18, pp. 42–75, Sept. 1998.

27. Ruther, W. E., W. K. Soppet, T. F. Kassner, and W. J. Shack, "Environmentally Assisted Cracking of Alloys 600 and 690 in Simulated LWR Water," Environmentally Assisted Cracking in Light Water Reactors, Semiannual Report, January 1998–July 1998, NUREG/CR–4667, Vol. 26, ANL–98/18, pp. 25–32, March 1999.

28. Ruther, W. E., W. K. Soppet, T. F. Kassner, and W. J. Shack, "Environmentally Assisted Cracking of Alloys 600 and 690 in Simulated LWR Water," Environmentally Assisted Cracking in Light Water Reactors, Semiannual Report, July 1998–December 1998, NUREG/CR–4667, Vol. 27, ANL–99/11, pp. 45-54, October 1999.

29. Soppet, W. K., O. K. Chopra, and W. J. Shack, "Environmentally Assisted Cracking of Alloys 600 and 690 in Simulated LWR Water," Environmentally Assisted Cracking in Light Water Reactors, Semiannual Report, July 1999–December 1999, NUREG/CR–4667, Vol. 29, ANL–00/23, pp. 39-45, November 2000.

30. Chopra, O. K., W. K. Soppet, and W. J. Shack, "Effects of Alloy Chemistry, Cold Work, and Water Chemistry on Corrosion Fatigue and Stress Corrosion Cracking of Nickel Alloys and Welds," NUREG/CR–6721, ANL–01/07, April 2001.

31. Cassagne, T. B., and A. Gelpi, "Crack Growth Rate Measurements on Alloy 600 Steam Generator Tubes in Steam and Primary Water," Proc. of the Fifth Intl. Symp. on Environmental Degradation of Materials in Nuclear Power Systems-Water Reactors, American Nuclear Society, La Grange Park, IL, pp. 518–524, 1991.

32. Foster, J. P., W. H. Bamford, and R. S. Pathania, "Initial Results of Alloy 600 Crack Growth Rate Testing in a PWR Environment," Proc. of the Seventh Intl. Symp. on Environmental Degradation of Materials in Nuclear Power Systems-Water Reactors, NACE International, Houston, TX, pp. 25–39, 1995.

33. Magdowski, R., F. Vaillant, C. Amzallag, and M. O. Speidel, "Stress Corrosion Crack Growth Rates of Alloy 600 in Simulated PWR Coolant," Proc. of the 8th Intl. Symp. on Environmental Degradation of Materials in Nuclear Power Systems-Water Reactors, S. M. Bruemmer, ed., American Nuclear Society, La Grange Park, IL, pp. 333–338, 1997.

34. Le Hong, S., C. Amzallag, and A. Gelpi, "Modeling of Stress Corrosion Crack Initiation on Alloy 600 in Primary Water of PWRs," Proc. of the Ninth Intl. Symp. on Environmental Degradation of Materials in Nuclear Power Systems-Water Reactors, F. P. Ford, S. M. Bruemmer, and G. S. Was, eds., Minerals, Metals, and Materials Society, Warrendale, PA, pp. 115–122, 1999.

35. Raquet, O., and G. Santarini, "Stress Corrosion Crack Propagation Rate of Alloy 600 in the Primary Water of PWR Influence of a Cold Worked Layer," Proc. of the Ninth Intl. Symp. on Environmental Degradation of Materials in Nuclear Power Systems-Water Reactors, F. P. Ford, S. M. Bruemmer, and G. S. Was, eds., Minerals, Metals, and Materials Society, Warrendale, PA, pp. 207–213, 1999.

36. White, G. A., Hickling, J., and Mathews, L. K., "Crack Growth Rates for Evaluating PWSCC of Thick–Wall Alloy 600 Material," Proc. of the 11th Intl. Symp. on Environmental Degradation of Materials in Nuclear Power Systems-Water Reactors, NACE International, Houston, TX, pp. 166–179, 2003.

37. White, G., J. Hickling, and C. Harrington, "MRP Development of Crack Growth Rate Disposition Curves for Primary Water Stress Corrosion Cracking (PWSCC) of Thick-Section Alloy 600 Components and Alloy 82, 182 and 132 Weldments," 2005 EPRI International PWSCC of Alloy 600 Conference, Santa Ana Pueblo, NM, March 7–10, 2005.

38. Macdonald, D. D., A. C. Scott, and P. Wentrcek, "External Reference Electrodes for Use in High Temperature Aqueous Systems," J. Electrochem. Soc. 126, pp. 908–911, 1979.

39. Andresen, P. L., and P. G. Campbell, "The Effects of Crack Closure in High–Temperature Water and its Role in Influencing Crack Growth Data," Proc. of the Fourth Intl. Symp. on Environmental Degradation of Materials in Nuclear Power Systems-Water Reactors, D. Cubicciotti, ed., NACE International, Houston, TX, pp. 4.86–4.111, 1990.

40. Alexandreanu, B., and G. S. Was, "A Priori Determination of the Sampling Size for Grain Boundary Character Distribution and Grain Boundary Degradation Analysis," Phil. Mag. A, 81 (8), pp. 1951–1965, 2001.

41. Briant, C. L., and E. L. Hall, "The Microstructural Causes of IG Corrosion of Alloys 82 and 182," Corrosion 43, pp. 539–548, 1987.

42. Alexandreanu, B., and G. S. Was, "Grain Boundary Deformation–Induced Intergranular Stress Corrosion Cracking of Ni-16Cr-9Fe in 360°C Water," Corrosion 59 (8), pp. 705, 2003.

43. Lindstrom, R., P. Lidar, and J. Lagerstrom, "Crack Growth of Alloy 182 in Simulated Primary Side PWR Environment," Proc. of the 8th Intl. Symp. on Environmental Degradation of Materials in Nuclear Power Systems-Water Reactors, S. M. Bruemmer, ed., American Nuclear Society, La Grange Park, IL, pp. 422–429, 1997.

44. Amzallag, C., G. Baudry, and J. L. Bernard, "Effects of PWR Environment on the Fatigue Crack Growth of Different Stainless Steels and Inconel Type Alloy," Proc. of the IAEA-Specialists Meeting on Subcritical Crack Growth, NUREG/CP–0044, Vol. 1, pp. 263–294, 1983.

45. Van Der Sluys, W. A., B. A. Young, and D. Doyle, "Corrosion Fatigue Properties on Alloy 690 and Some Nickel–Based Weld Metals," Assessment Methodologies for Preventing Failure: Service Experience and Environmental Considerations, PVP Vol. 410-2, R. Mohan, ed., American Society of Mechanical Engineers, New York, pp. 85–91, 2000.

46. Psaila–Dombrowski, M. J., C. S. Wade, J. M. Sarver, W. A. Van Der Sluys, and P. E. Doherty, "Evaluation of Weld Metals 82, 152, 52, and Alloy 690 Stress Corrosion Cracking and Corrosion Fatigue Susceptibility," Proc. of the 8th Intl. Symp. on Environmental Degradation of Materials in Nuclear Power Systems-Water Reactors, S. M. Bruemmer, ed., American Nuclear Society, La Grange Park, IL, pp. 412–421, 1997.

47. James, L. A., and W. J. Mills, "Fatigue–Crack Propagation Behavior of Wrought Alloy 600 and Weld–Deposited EN82H in an Elevated Temperature Aqueous Environment," Service Experience, Structural Integrity, Severe Accident, and Erosion in Nuclear and Fossil Plants, PVP Vol. 303, American Society of Mechanical Engineers, pp. 21–36, 1995.

48. Bamford, W. H., J. P. Foster, and R. S. Pathania, "An Investigation of Alloy 182 Stress Corrosion Cracking in Simulated PWR Environment," Proc. of the Ninth Intl. Symp. on Environmental Degradation of Materials in Nuclear Power Systems-Water Reactors, F. P. Ford, S. M. Bruemmer, and G. S. Was, eds., Minerals, Metals, and Materials Society, Warrendale, PA, pp. 279–294, 1999.

49. Bamford, W. H., J. P. Foster, K. R. Hsu, L. Tunon–Sanur, and A. McIlree, "Alloy 182 Weld Crack Growth, and Its Impact on Service–Induced Cracking in Operating PWR Plant Piping," Proc. Tenth Intl. Conf. on Environmental Degradation of Materials in Nuclear Power Systems-Water Reactors, NACE International, Houston, TX, 2001.

50. Le Hong, S., J. M. Boursier, C. Amzallag, and J. Daret, "Measurement of Stress Corrosion Cracking Growth Rates in Weld Alloy 182 in Primary Water of PWR," Proc. of the Tenth Intl. Conf. on Environmental Degradation of Materials in Nuclear Power Systems-Water Reactors, NACE International, Houston, TX, 2001.

51. Cassagne, T., D. Caron, J. Daret, and Y. Lefevre, "Stress Corrosion Crack Growth Rate Measurements in Alloys 600 and 182 in Primary Loops Under Constant Load," Proc. of the Ninth Intl. Symp. on Environmental Degradation of Materials in Nuclear Power Systems-Water Reactors, F. P. Ford, S. M. Bruemmer, and G. S. Was, eds., Minerals, Metals, and Materials Society, Warrendale, PA, pp. 217–224, 1999.

52. Magdowski, R., and M. Speidel, "Stress Corrosion Crack Growth of Weld Material Alloy 182 in Simulated PWR Environments," Institute of Metallurgy, Swiss Federal Institute, Internal Report No. 226, Zurich, Jan. 2001.

53. Jacko, R. J., R. E. Gold, G. V. Rao, K. Koyama, and A. Kroes, "Results of Accelerated SCC Testing of Alloy 82, Alloy 182 and Alloy 52M Weld Metals," NUREG/CP-0191, The Vessel Penetration Inspection, Crack Growth and Repair Conference, Oct. 2, 2003, Gaithersburg, MD, Vol. 1, pp. 413–426, 2003.

54. Attanasio, S., J. V. Mullen, J. W. Wuthrich, W. W. Wilkening, and D. S. Morton, "Stress Corrosion Crack Growth Rates (SCCGRs) for Alloy 182 and 82 Welds," NUREG/CP-0191, The Vessel Penetration Inspection, Crack Growth and Repair Conference, Oct. 2, 2003, Gaithersburg, MD, Vol. 1, pp. 267–296, 2003.

55. Brown, C. M., and W. J. Mills, "Effect of Water on Mechanical Properties and Stress Corrosion Behavior of Alloy 600, Alloy 690, EN82H Welds, and EN52 Welds," Corrosion 55 (2), pp. 173–186, 1999.

56. Mills, W. J., and C. M. Brown, "Stress Corrosion Crack Growth Rates for Alloy 82H Welds in High Temperature Water," Proc. of the 11th Intl. Conf. on Environmental Degradation of Materials in Nuclear Power Systems-Water Reactors, NACE International, Houston, TX, 2003.

57. Tsutsumi, K., H. Kanasaki, K. Yoshimoto, Y. Nomura, S. Asada, and T. Yonezawa, "SCC Growth Rate of Nickel Based Alloy 132 Weld Metal in PWR Water," Proc. of the 11th Intl. Conf. on Environmental Degradation of Materials in Nuclear Power Systems-Water Reactors, NACE International, Houston, TX, 2003.

58. Webb, G. L., and M. G. Burke, "Stress Corrosion Cracking Behavior of Ally 600 in High–Temperature Water," Proc. of the 7th Intl. Symp. on Environmental Degradation of Materials in Nuclear Power Systems-Water Reactors, NACE International, Houston, TX, pp. 41–55, 1995.

NRC FORM 335 (9-2004) NRCMD 3.7	U. S. NUCLEAR REGULATORY COMMISSION	1. REPORT NUMBER (Assigned by NRC. Add Vol., Supp., Rev., and Addendum Numbers, if any.)
BIBLIOGRAPHIC DATA SHEET *(See instructions on the reverse)*		NUREG/CR– 6921 ANL—05/55

2. TITLE AND SUBTITLE	3. DATE REPORT PUBLISHED	
Crack Growth Rates in a PWR Environment of Nickel Alloys from the Davis-Besse and V.C. Summer Power Plants	MONTH November	YEAR 2006
	4. FIN OR GRANT NUMBER Y6388	

5. AUTHOR(S)	6. TYPE OF REPORT Technical; Topical
B. Alexandreanu, O. K. Chopra, and W. J. Shack	7. PERIOD COVERED *(Inclusive Dates)*

8. PERFORMING ORGANIZATION – NAME AND ADDRESS *(If NRC, provide Division, Office or Region, U.S. Nuclear Regulatory Commission, and mailing address; if contractor, provide name and mailing address.)*

Argonne National Laboratory
9700 South Cass Avenue
Argonne, IL 60439

9. SPONSORING ORGANIZATION – NAME AND ADDRESS *(If NRC, type "Same as above"; if contractor, provide NRC Division, Office or Region, U.S. Nuclear Regulatory Commission, and mailing address.)*

Division of Fuel, Engineering & Radiological Research
Office of Nuclear Regulatory Research
U.S. Nuclear Regulatory Commission
Washington, DC 20555–0001

10. SUPPLEMENTARY NOTES
William H. Cullen, Jr., NRC Project Manager

11. ABSTRACT (200 words or less)

In light water reactors (LWRs), vessel internal components made of nickel–base alloys are susceptible to environmentally assisted cracking. A better understanding of the causes and more effective mechanisms of this cracking may permit more accurate assessments of damage accumulation and requirements on inspection intervals. A program is under way at Argonne National Laboratory to evaluate the resistance of Ni alloys and their welds to environmentally assisted cracking in simulated LWR coolant environments. This report presents crack growth rate (CGR) results for the following nickel alloys tested in a simulated LWR environment: Alloy 600 removed from the Davis–Besse control rod drive mechanism nozzle #3, Alloy 182 from a J–groove weld nozzle #11 from Davis–Besse, and Alloys 182 and 82 from a hot–leg nozzle–to–pipe weld of the V.C. Summer reactor coolant system. The results from the present study are compared with the existing CGR data for Ni alloys to determine the relative susceptibility of these particular heats of material to environmentally enhanced cracking. Under cyclic loading, the Alloy 600 nozzle exhibited significant environmental enhancement, but little or no environmental enhancement was evident for the weld alloys from both Davis-Besse and V.C. Summer. Under constant load, the CGRs of the Alloy 600 nozzle are a factor of 4–8 higher than the median CGRs based on all the available data for Alloy 600 materials. This material exhibited predominantly intergranular fracture, even during precracking under cyclic loads. For both the Davis-Besse and V.C. Summer weld alloys, the CGRs under constant load are lower than those predicted by the disposition curve proposed for Alloy 182 weld metals.

12. KEY WORDS/DESCRIPTORS *(List words or phrases that will assist researchers in locating this report.)*	13. AVAILABILITY STATEMENT unlimited
Primary water stress corrosion cracking Ni-alloy weld metals Alloy 600 V. C. Summer nozzle-to-pipe weld Davis Besse CRDM nozzle alloy Crack growth rate	14. SECURITY CLASSIFICATION *(This Page)* unclassified
	(This Report) unclassified
	15. NUMBER OF PAGES
	16.PRICE

Printed
on recycled
paper

Federal Recycling Program

UNITED STATES
NUCLEAR REGULATORY COMMISSION
WASHINGTON, DC 20555-0001

OFFICIAL BUSINESS